

**NONLINEAR DYNAMICS  
OF HODGKIN-HUXLEY NEURONS**



UNIWERSYTET IM. ADAMA MICKIEWICZA W POZNANIU

SERIA FIZYKA NR 83

LECH S. BORKOWSKI

**NONLINEAR DYNAMICS  
OF HODGKIN-HUXLEY NEURONS**



POZNAŃ 2010

ABSTRACT. Lech S. Borkowski, *Nonlinear dynamics of Hodgkin-Huxley neurons* [Dynamika nieliniowa neuronów Hodgkina-Huxleya], Adam Mickiewicz University Press. Poznań 2010. Seria Fizyka nr 83. Pp. 78, figures 71. ISBN 978-83-232-2106-7. ISSN 0554-825X.

This monograph describes the dynamics of the Hodgkin-Huxley neurons stimulated by periodic and stochastic stimuli. In the high frequency regime there is a multimodal transition between the odd-only modes and the state with both odd and even modes. This singularity appears in the presence of noise as a stochastic anti-resonance. The competition of different parity modes is also reflected in the structure of the resonances, where even and odd phase-locked states are separated by crossover regimes. The boundaries between various mode-locked states form complicated patterns. The relation between the output frequency and stimulus amplitude near the excitation threshold is often continuous even in the absence of noise. Several scaling relations are found. Models of regular spiking excitatory and inhibitory cells of mammalian cortex are also studied within this framework. The obtained high variability of response agrees with experiments *in vivo*.

Lech S. Borkowski, Wydział Fizyki, Uniwersytet im. Adama Mickiewicza (Faculty of Physics, Adam Mickiewicz University), ul. Umultowska 85, 61-614 Poznań, Poland

Recenzent: prof. dr hab. M. R. Dudek

© Copyright by Lech S. Borkowski 2010

© Copyright for this edition by Wydawnictwo Naukowe UAM, Poznań 2010

Projekt okładki: Lech S. Borkowski

Redakcja techniczna: Dorota Borowiak

ISBN 978-83-232-2106-7

ISSN 0554-825X

WYDAWNICTWO NAUKOWE UNIWERSYTETU IM. ADAMA MICKIEWICZA W POZNANIU  
61-734 Poznań, ul. F. Nowowiejskiego 55,  
tel. +48 61 829 39 85, fax +48 61 829 39 80  
e-mail: [press@amu.edu.pl](mailto:press@amu.edu.pl) <http://amu.edu.pl/~press>

Wydanie I. Ark. wyd. 6,25. Ark. druk. 4,875

Druk i oprawa: ZAKŁAD GRAFICZNY UAM, POZNAŃ, UL. WIENIAWSKIEGO 1

# Contents

<b>1. Introduction</b>	7
<b>2. High-frequency response</b>	9
2.1. Introduction	9
2.2. The model	10
2.3. Results	12
2.4. Discussion	19
2.5. The even-all multimodal transition	20
<b>3. Resonance</b>	25
3.1. Introduction	25
3.2. Results	26
3.3. The quasi-discrete return map	33
<b>4. Noise</b>	35
4.1. Introduction	35
4.2. Sensitivity of the firing rate to noise	36
4.3. Stochastic anti-resonance	40
4.4. Scaling near the edges of the mode-locked states	42
4.5. Poisson input	45
<b>5. Pulse packets</b>	46
5.1. Response to an isolated spike	46
5.2. Response to a cluster of spikes	47
<b>6. The Hodgkin-Huxley network</b>	50
<b>7. Regular spiking cortical cells</b>	58
7.1. Introduction	58
7.2. Regular spiking excitatory neuron	60
7.3. Regular spiking inhibitory neuron	63
7.4. Poisson input	67
<b>8. Summary</b>	72
<b>Bibliography</b>	75



# 1. Introduction

The general mechanism of electric impulse conduction through nerve cells was first successfully explained by Hodgkin and Huxley [Hodgkin and Huxley, 1952]. Selective transport of ions through the cellular membrane is possible due to the existence of ionic channels. The current through an ion channel often satisfies the Ohm's law, where,

$$I = g_{channel}(V)(V - E_{channel}), \quad (1.1)$$

where  $g_{channel}$  is the voltage dependent (or ligand concentration dependent) channel conductance and  $E_{channel}$  is the reversal potential of the channel.

The crucial ingredient of the Hodgkin-Huxley (HH) theory is the qualitatively correct model of conductances of the dominant sodium and potassium ion channels. Using a phenomenological analysis they proposed that

$$g_{Na} = \bar{g}_{Na}m^3h, \quad (1.2)$$

and

$$g_K = \bar{g}_Kn^4, \quad (1.3)$$

where  $\bar{g}_{Na}$ ,  $\bar{g}_K$  are the maximal sodium and potassium conductances,  $m$  is the probability of a Na channel gate being open, and  $h$  - the probability that another gate does not block this channel. We will use a simplified notation throughout this work, replacing  $\bar{g}_{channel}$  with  $g_{channel}$  as the maximal conductance. The combined action of three independent gates  $m$  and one  $h$  is needed for the Na channel to be in the open state. For the potassium channel four independent gates may be in the open position with probability  $n$ . This prediction was later confirmed microscopically, initially for the potassium channel [Doyle et al., 1998].

The simplest Markov kinetic scheme for the Na<sup>+</sup> channel requires eight states. The simplest linear kinetic scheme for the delayed rectifier K<sup>+</sup> channel requires five states. The detailed description of time dependence of transition rates between different channel states involves a large number of variables that are not

easy to obtain from experiment. Therefore the typical approach is limited to the first-order kinetics.

The HH model does not describe properly the kinetics of the inactivation of the sodium channel [Bezanilla and Armstrong, 1977, Armstrong and Bezanilla, 1977, Clay, 1998]. It does not account for the channel noise and cannot be used for small patches of cellular membranes, of order  $\mu\text{m}^2$  or less, where the stochastic nature of the gating processes cannot be neglected [Strassberg and DeFelice, 1993, Mainen and Sejnowski, 1995, Schneidman et al., 1998, Schmid et al., 2001]. It is however sufficiently reliable as a generic model of a nerve cell excitability. It has e.g. resonant properties and is a useful generic model for studying phenomena such as stochastic resonance. Due to strong nonlinearities of the model the solution can be obtained only by numerical simulation.

The HH model is also the convenient starting point for other conductance-based models derived from it, where the aim is to provide description of various phenomena, e.g. inhibition and bursting, including dependence on the concentration of ions, most notably  $\text{Ca}^{2+}$ .

We study the reaction of the model neuron to a set of short conductance pulses. While both the constant and time-varying stimuli were used in many of the past studies, we believe this work substantially improves our understanding of the dynamics of one of the fundamental models used in neuroscience. We start in Chapter 2 by analyzing the multimodal nature of the spectrum in response to a perfectly periodic input, paying particular attention to the parity of the response modes. The nature of the HH neuron's resonant response and the behavior in the perithreshold regime is studied in Chapter 3. The addition of noise to the periodic signal in Chapter 4 significantly alters the behavior of the neuron and lowers the excitation threshold. The existing deterministic resonances and anti-resonances continue to dominate the stochastic response in a somewhat altered form of stochastic resonance and stochastic anti-resonance. The influence of the detailed time dependence of a single pulse or cluster of pulses on the excitation threshold is reviewed in Chapter 5, where we find scaling in the limit of short stimuli. The behavior of networked HH neurons is studied in Chapter 6. Finally in Chapter 7 we look at an extension of the HH model to excitatory and inhibitory cortical cells commonly encountered in mammals, where we describe the neuron response and try again to identify forms of resonant behavior.

The stimulus amplitude is expressed in terms of the maximal synaptic conductance  $g_{syn}$  throughout this work. The HH model is current-driven in Chapters 2 and 3, Sections 4.3 and 4.4, Chapters 5 and 7. The model is conductance-driven in Sections 4.3, 4.5 and in Chapter 6.

## 2. High-frequency response

*Sections 2.1-2.4 reprinted with permission from L. S. Borkowski, Physical Review E 80, 051914 (2009). Copyright 2009 by the American Physical Society.*

### 2.1. Introduction

Biological neurons transmit information in the form of sharp spikes of potential difference across the lipid bilayer forming the wall of the nerve cell. This feature of the cell's reaction to input signals is remarkably consistent in different organisms and different types of neurons. The action potential spikes are assumed to be the principal carrier of information. The early view that information is transmitted via rate coding has evolved. It is now recognized that also the spike time coding is used in neural systems [Sejnowski, 1995, Ferster and Spruston, 1995]. While the precise coding recipe is unknown it is clear that the knowledge of the response of various types of neurons to different stimuli is fundamental to formulating the theory of information transfer in the neural system.

Our understanding of conductance-based models of neurons is largely based on the Hodgkin-Huxley (HH) model originally formulated to describe the dynamics of the membrane potential of the squid giant axon [Hodgkin and Huxley, 1952]. The detailed voltage-clamp measurements of the voltage-gated potassium and sodium ion currents led to revisions of the HH model. The modifications required to achieve better agreement with experiments were reviewed by Clay [Clay, 2005]. Studies of single neurons and neuronal networks often employ simplified models, such as integrate-and-fire and FitzHugh-Nagumo (FHN) models [Gerstner, 1995, Bressloff and Coombes, 1998]. It is believed that the two-dimensional flow models such as FHN reproduce qualitatively the behavior of the HH model. However these simplifications are not always justifiable [Rinzel and Miller, 1980, Brown et al., 1999, Guckenheimer and Oliva, 2002]. In an interesting analysis of chaos in the HH model Guckenheimer and Oliva [Guckenheimer and Oliva, 2002] pointed out that even the concept of a firing threshold may be more subtle than just a smooth hypersurface dividing subthreshold and suprathreshold membrane potentials.

Over the years many studies of HH equations were carried out, including stochastic variations of various quantities [Lee and Kim, 1999, Pankratova et al.,

2005, Luccioli et al., 2006]. An important question is to what extent the qualitative properties of neuron response depend on the functional form of the input signal. One frequently used form of input is constant plus a sinusoidal term. However the physiological signals are more pulse-like. In a strongly nonlinear system this may lead to substantial differences in the output.

In the sinusoidally driven HH model the excitation threshold rises sharply at large frequencies. The phase diagram in the frequency-current amplitude plane consists of three phase locked regions with integer ratio of the output period to the input period,  $\bar{T}_o/T_i$ , 1:1, 2:1, and 3:1. There are also areas of fractional locking and bistable or chaotic response around these phase-locked states [Lee and Kim, 2006, Chik et al., 2001, Che et al., 2009].

It was pointed out that the edges of mode-locked plateaus have analogies to phase transitions in the equilibrium statistical mechanics. Two forms of scaling of the average deviation from perfect mode-locking were found near the edges of plateaus with constant  $p/q$ , where  $p$  and  $q$  are integers, indicating number of input spikes per number of output action potentials [Engelbrecht and Mirolo, 2009]. The scaling has either exponent 1/2 or is logarithmic. In this paper we will show that scaling is more common and appears also near the multimodal transition points.

Here we assume the  $\alpha$ -form of postsynaptic current,  $I_{syn} \sim t \exp(-t/\tau)$ , where  $t$  is time from the onset of the input spike and  $\tau$  is the time scale of the synaptic action. This form is close to experimental observation although it does not take into account a more complex dynamics of the ion channel kinetics, usually described in the Markovian scheme.

The general form of the phase diagram of the Hodgkin-Huxley model with this input was studied initially in Ref. [Hasegawa, 2000]. However many important questions are still to be answered. One of them is the behavior of the system in the high-frequency limit. In the following we present the model and show the main features of high-frequency response.

## 2.2. The model

The Hodgkin-Huxley neuron subject to periodic conductance pulses is defined by the following set of equations [Hodgkin and Huxley, 1952]:

$$CdV/dt = -g_{Na}m^3h(V - V_{Na}) - g_Kn^4(V - V_K) - g_L(V - V_L) + I_{ext} + I_{syn}, \quad (2.1)$$

$$dm/dt = -(a_m + b_m)m + a_m, \quad (2.2)$$

$$dh/dt = -(a_h + b_h)h + a_h, \quad (2.3)$$

$$dn/dt = -(a_n + b_n)n + a_n, \quad (2.4)$$

where

$$a_m = 0.1(V + 40)/[1 - e^{-(V+40)/10}], \quad (2.5)$$

$$b_m = 4e^{-(V+65)/18}, \quad (2.6)$$

$$a_h = 0.07e^{-(V+65)/20}, \quad (2.7)$$

$$b_h = 1/[1 + e^{-(V+35)/10}], \quad (2.8)$$

$$a_n = 0.01(V + 55)/[1 - e^{-(V+55)/10}], \quad (2.9)$$

$$b_n = 0.125e^{-(V+65)/80}. \quad (2.10)$$

In equations (2.5)-(2.10) the voltage is expressed in mV and the rate constants  $a$  and  $b$  are given in  $\text{ms}^{-1}$ . The reversal potentials of sodium, potassium and leakage channels are  $V_{Na} = 50\text{mV}$ ,  $V_K = -77\text{mV}$ , and  $V_L = -54.5\text{mV}$ , respectively. The corresponding maximum conductances are  $g_{Na} = 50\text{mS}$ ,  $g_K = 36\text{mS/cm}^2$ , and  $g_L = 0.3\text{mS/cm}^2$ . The capacity of the membrane is  $C = 1\mu\text{F/cm}^2$  [Hodgkin and Huxley, 1952].

The synaptic current  $I_{syn}$  is given by the following equation,

$$I_{syn}(t) = g_{syn} \sum_n \alpha(t - t_{in})(V_a - V_{syn}), \quad (2.11)$$

where  $t_{in}$  denotes the start of the  $n^{\text{th}}$  pulse,  $g_{syn}$  is the conductivity of the synapse,  $V_a = 30\text{mV}$  is the maximum potential in the postsynaptic area and  $V_{syn} = -50\text{mV}$  is the reversal potential of the synapse. The period of the synaptic drive is  $T_i = t_{in+1} - t_{in}$ . The external current  $I_{ext}$  is set to 0, except for a sample run shown in Fig. 2.1.

The time-dependence is given by the function

$$\alpha(t) = (t/\tau)e^{-t/\tau}\Theta(t), \quad (2.12)$$

where  $\tau$  is time scale characterizing the dynamics of the synaptic action and  $\Theta(t)$  is the Heaviside step function. We study the dependence of the output interspike separation  $T_o$  on  $T_i$  and  $g_{syn}$ .

Equations (2.1)-(2.10) were integrated with the fourth order Runge-Kutta scheme. The time step was 0.01 ms. For each parameter set the simulation was run for 30 seconds. Results of the initial three seconds of each data set were discarded to avoid transient behavior. In the chaotic regime the data shown in Figs. 5, 7-9, and 11 were obtained from five runs for each value of the horizontal coordinate. Fig. 2.6 includes results of 100 runs for each  $T_i$ .

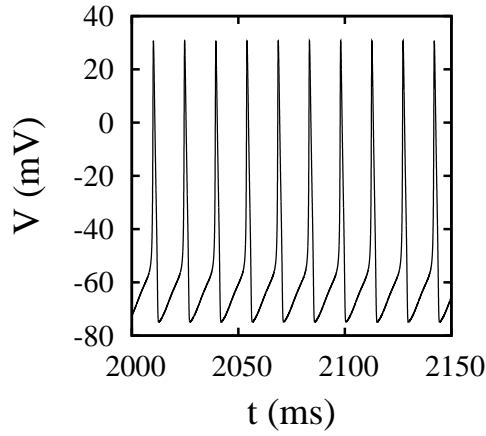


Figure 2.1: Sample voltage trace of the Hodgkin-Huxley model for a constant input current  $I_{ext} = 10\mu\text{A}/\text{cm}^2$ .

### 2.3. Results

The average output spiking rate in the form of a color map as a function of the input period  $T_i$  and maximum synaptic conductivity  $g_{syn}$  is presented in Fig. 2.2. The mode-locked regions are shown as areas of uniform color.

For small  $T_i$  the total incoming current is approximately constant with a small modulation, and the excitation threshold rises linearly with increasing  $T_i$ ,  $g_{syn} \approx 0.04T_i$  mS/(ms cm<sup>2</sup>). For  $g_{syn}$  exceeding approximately  $0.4T_i$  mS/(ms cm<sup>2</sup>) the spiking action does not occur. We can see from Fig. 2.2 that this behavior sets in below  $T_i \approx 6$ ms .

The obtained phase diagram is qualitatively different from a response to a sinusoidal input, where the excitation threshold diverges as  $1/T_i$ , for  $T_i \rightarrow 0$ . In general we may expect that the constraint of charge balancing,  $\int_t^{t+T_i} Idt = 0$ , will have a significant impact at high frequencies. For intermediate values of the input period,  $5\text{ms} < T_i < 13\text{ms}$ , the topology of the phase diagram resembles results obtained with sinusoidal input (see, e.g., Fig. 2 of Ref. [Lee and Kim, 2006]).

Fig. 2.3 shows dependence of minima and maxima of  $V$  on  $g_{syn}$  for three input frequencies. The amplitude of response decreases linearly with increasing  $g_{syn}$ . There is no well-defined spiking threshold. There are intervals of parameter values for which the response is highly irregular and the values of maxima and minima of  $V$  vary significantly.

A sample time-dependence of the membrane potential is shown in Fig. 2.4. The maxima of  $V$  span almost the entire range between  $-60\text{mV}$  and  $0\text{mV}$ . There is no clear separation of spikes from the rest of the signal.

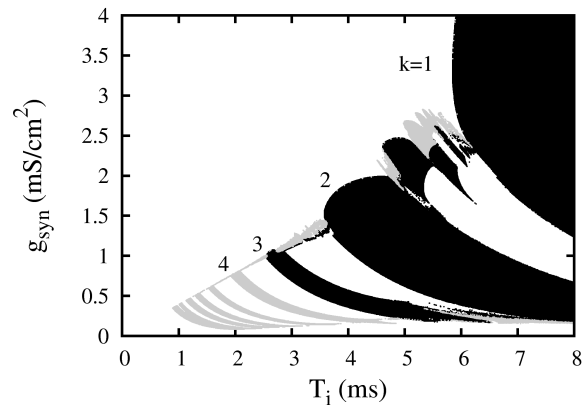


Figure 2.2: The ratio of the average output spiking rate to the input rate,  $k = \bar{T}_o/T_i$ . Mode-locked regions with  $k = 1, 2, 3$  and  $k = 4, 5, 6, 7, 8$  are shown in black and grey respectively. Voltage peaks were counted as spikes when  $V$  exceeded 0. For high values of  $g_{syn}$  the neuron does not respond.

Chaotic behavior in the parameter space between the 3:1 and 2:1 mode-locked regions leads to multimodal response. The interspike separation for  $g_{syn} = 0.4\text{mS}/\text{cm}^2$  is shown in Fig. 2.5. For  $T_i$  between 5.5ms and 6ms all integer multiples of input  $T_i$  with the exception of the lowest one appear in the output interspike interval histogram (ISIH).

It is interesting to note that ISIHs from some older experiments on nerve fibers of monkeys [Rose et al., 1967] and single neurons in the primary visual cortex of a cat [Siegel, 1990] show some similarities to Fig. 2.5. Experimental histograms are sequences of diminishing peaks occurring at integer multiples of the input interspike separation. In Fig. 2.5 the lowest element of the sequence is missing due to the refractoriness of the neuron. Similar form of ISIH was obtained in a theoretical study of a bistable system stimulated by periodic function with additive Gaussian noise [Longtin et al., 1991], where the presence of noise was essential. However the multimodal histogram was also obtained in a simulation of a deterministic modification of the HH model [Clay, 2003].

The HH model studied here does not contain stochastic terms. The multimodal response in Fig. 2.5 is a result of a deterministic nonlinearity. Thus noise is not the only ingredient enabling the reproduction of the multimodal experimental ISIH. It is possible to identify the source of multimodality by studying ISIH in more detail.

Close to the excitation threshold, at  $g_{syn} \approx 0.2\text{mS}/\text{cm}^2$ , there exists a transition from the odd-only ISIH to ISIH with all integer multiples of  $T_i$  (see Figs. 2.6 and 2.7). Near the transition the edges of high- $k$  clusters scale logarithmically. The scaling holds both along the  $T_i$  and  $g_{syn}$  axes. It can be viewed as a competition between the odd and the even multiples of the driving period.

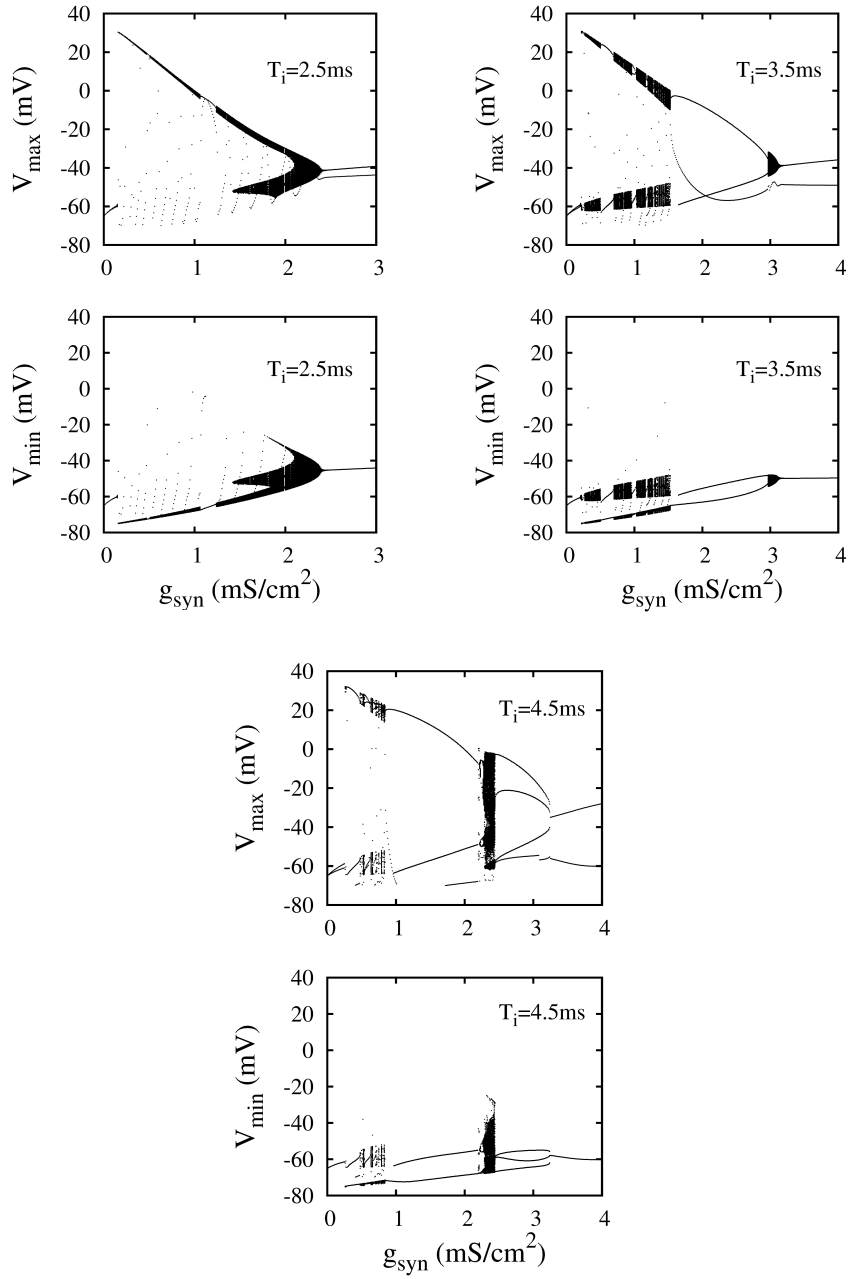


Figure 2.3: Values of maxima and minima of the membrane potential  $V(t)$  as a function of synaptic conductivity  $g_{\text{syn}}$  for input spike intervals  $T_i = 2.5\text{ms}$ ,  $3.5\text{ms}$ , and  $4.5\text{ms}$ .

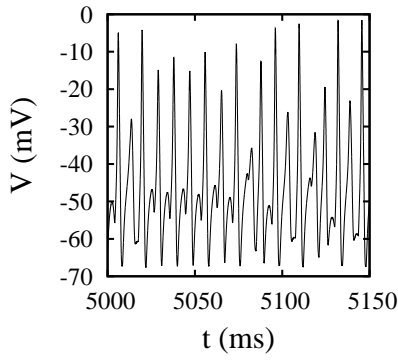


Figure 2.4: For high synaptic conductivities the distinction between action potential and the background oscillations loses its meaning. This sample was obtained for  $T_i = 4.5\text{ms}$  and  $g_{syn} = 2.35\text{mS/cm}^2$ .

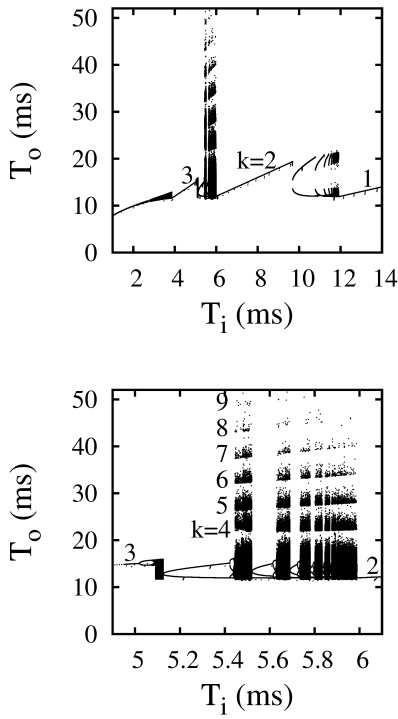


Figure 2.5: (Upper) The spectrum of interspike separations of the output signal as a function of the input period  $T_i$  for  $g_{syn} = 0.4\text{mS/cm}^2$ . (Lower) Detailed view of the chaotic region between  $T_i = 5\text{ms}$  and  $6\text{ms}$ . Each ISI cluster belongs to different  $k$ , where  $k = 2, 3, 4, 5, \dots$ . The distinction between  $k = 2$  and  $k = 3$  is blurred.

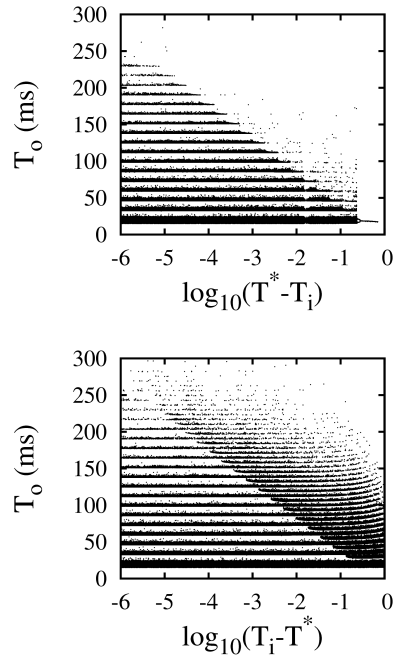


Figure 2.6: Scaling of the excitation edge of (upper) odd-only multiples of the input  $T_i$ , and (lower) all integer multiples, in the chaotic region between  $k = 2$  and  $k = 3$ . For  $g = 0.2\text{mS}/\text{cm}^2$ , the transition occurs at  $T = 6.54175\text{ms}$ .

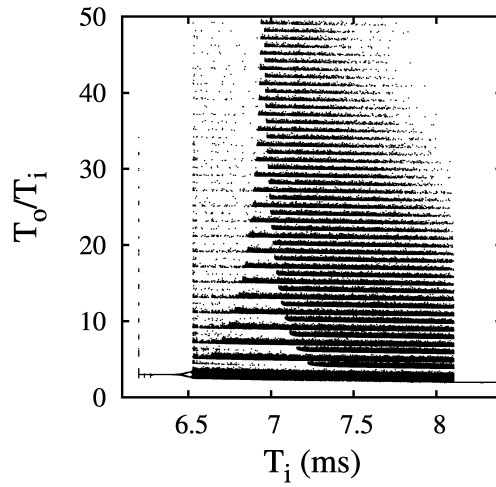


Figure 2.7: The transition between odd-only and all modes at  $g = 0.17\text{mS}/\text{cm}^2$ . Even modes are absent below the transition point.

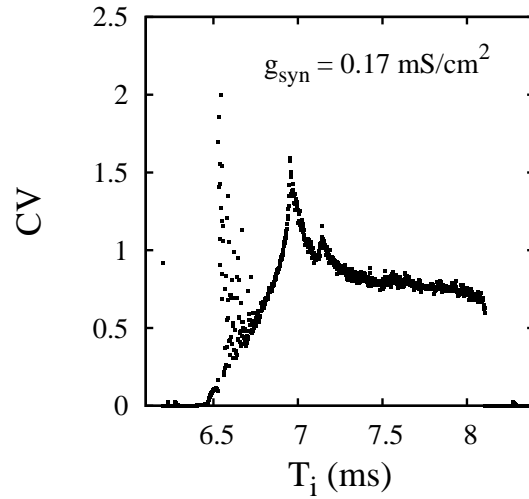


Figure 2.8: Coefficient of variation for  $g = 0.17\text{mS}/\text{cm}^2$ . The variability near  $T_i = 6.6\text{ms}$  is due to the proximity to the firing threshold.

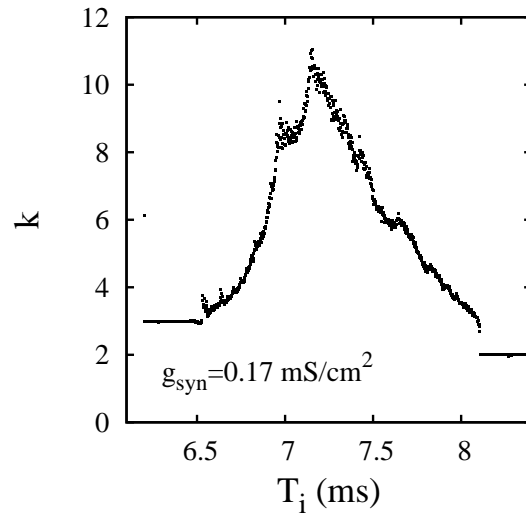


Figure 2.9: The ratio  $k = T_o/T_i$  for  $g = 0.17\text{mS}/\text{cm}^2$ . The maximum of  $k$  is shifted approximately 0.2 ms to the right relative to maximum of CV (see Fig. 2.8).

A clear indication of this 'spectral' transition is the singular behavior of the coefficient of variation (CV), see Fig. 2.8. At the transition CV is of order 1 and  $k$  is significantly larger than 3. The maximum  $k$  occurs approximately 0.2ms above the singularity of CV (see Fig. 2.9). One may also think of this shift as a

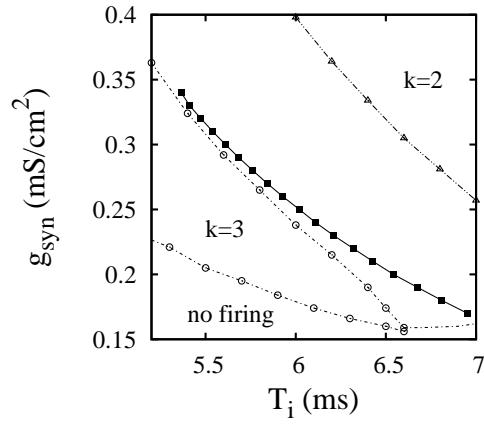


Figure 2.10: The location of the multimodal transition (filled squares) on the response diagram.

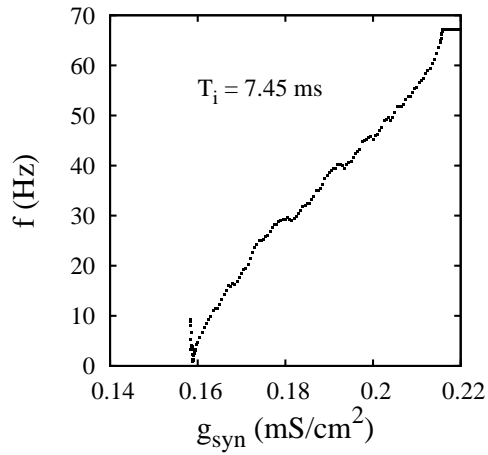


Figure 2.11: Frequency vs. synaptic conductivity for  $T_i = 7.45$ ms. Each data point is averaged over 15 runs for 60 s with different initial conditions. The initial 6 s from each run were discarded.

result of relaxation from the constraint of odd-only modes below  $T^*$ . At  $T^*$  the highest even modes become available and this leads to the increase of  $k$ .

If such transition were found experimentally it would be a clear sign of the deterministic nonlinear dynamics. In the presence of noise this sharp feature would be smeared and would vanish if noise dominates the dynamics of the system.

## 2.4. Discussion

For high synaptic drives in the high frequency regime distinguishing the action potential from the background activity becomes problematic. In this limit the neuron is very sensitive to small changes of the functional form of the signal. For periodic drive with small time constant  $\tau$  and  $T_i$  below 6ms the width of the spiking regime along the  $g_{syn}$  axis scales linearly with  $T_i$ . The quality of the neuron's response deteriorates linearly with increasing  $g_{syn}$ . This is in contrast to findings for a sinusoidal signal, and more generally for a class of signals satisfying the constraint of charge balancing, where the spiking action remains well defined in the high-frequency limit.

A mechanism of suppression of the neuron's activity might help to explain self-regulating behavior of neocortical networks. Various mechanisms of homeostatic action for neural microcircuits were proposed [Muresan and Savin, 2007]. It would be useful to investigate whether more realistic extensions of the Hodgkin-Huxley model also exhibit self-regulation in response to high-frequency inputs. The network of such neurons would have a "safety switch" built in at the level of individual cells. For  $T_i$  between 4 and 6 ms the upper critical synaptic conductivity is of order  $2\text{mS}/\text{cm}^2$ , which is in the realistic range for neocortical pyramidal neurons [Ho and Destexhe, 2000].

The input ISI of 4 – 8ms is important to understanding the dynamics of the Hodgkin-Huxley model. In the chaotic region between the  $k = 2$  and  $k = 3$  locked states the coefficient of variation of ISI has a singularity at the transition between the odd-only and all-integer multiples of the driving period. The odd modes dominate in the vicinity of the  $k = 3$  state (see Fig. 2.10). The low- $k$  (high-frequency) bands vanish logarithmically near the line of critical points  $(g_{syn}, T^*)$ . The firing rate has a minimum at  $T_i \simeq T^* + 0.2\text{ms}$ . Periodically stimulated giant axons of squid have similar nonmonotonic dependence of the firing rate on the current pulse amplitude between the  $k = 2$  and  $k = 3$  states [Takahashi et al., 1990]. This experiment also showed linear dependence of the firing rate on pulse amplitude near the threshold for  $T_i > T^*$ , similarly to Fig. 2.11. Although the experimental pulses were rectangular, different from the  $\alpha(t)$  form with an exponential tail, the qualitative features do not depend much on the precise shape of a pulse. For short pulses the neuron's reaction is determined mainly by the time integral of the stimulus.

The multimodal response occurring in certain sensory neurons may result from noise [Longtin et al., 1991] or deterministic nonlinearity [Kaplan et al., 1996]. It would be interesting to look for experimental evidence of the odd-all transition. If found, it would be a clear evidence that the neuron dynamics is dominated by nonlinearity, not noise.

The behavior of the model at small  $T_i$  may be useful to both coincidence detection and estimation of the signal strength. The optimal sensitivity in this case is inversely proportional to frequency.

Our calculation also supports the view expressed by authors of Ref. [Guckenheimer and Oliva, 2002] that boundaries between various parts of the response diagram are not always clear-cut and may form complicated patterns. This statement also applies to the excitation threshold in the chaotic regime.

In the Hodgkin classification of intrinsic excitability [Hodgkin, 1948] class 1 neurons maintain firing at arbitrarily low frequencies in response to weak inputs and have continuous frequency-current ( $f-I$ ) curve. Class 2 neurons fire with certain relatively large frequency, usually of order 40-50 Hz, when stimulus exceeds the threshold and have a discontinuous  $f-I$  dependence. Classes 1 and 2 neurons sometimes are described as integrators and resonators, respectively [Izhikevich, 2000]. According to the commonly held view a neuron cannot be an integrator and resonator at the same time. However we showed that the deterministic HH neuron in a chaotic regime near the excitation threshold may oscillate with arbitrarily small frequencies and may perform integration at time scales much longer than the period of its main resonance. The character of the response depends strongly on the functional form of the stimulus and parameters of the model. A recent study showed that the same pyramidal neurons behave as integrators *in vitro* and resonators *in vivo* [Prescott et al., 2008].

The multimodal response of the HH neuron near 140-180 Hz is not a typical resonance since no particular frequency is preferred. The multiples of the driving frequency alternate chaotically. The average output frequency depends nonmonotonically on the stimulus amplitude. Similar nonmonotonic  $f$  vs  $I$  relation was found in periodically stimulated giant axons of squid [Takahashi et al., 1990]. Smaller stimuli favor higher multiples of the driving period. Studies of large neuronal networks of various types suggest that there may be a complex interplay between the integrating behavior and the resonant action [Muresan and Savin, 2007].

The ability to precisely control the nerve cell's potential oscillations is important in constructing devices performing the procedure known as deep brain stimulation [Benabid et al., 1991, Gross and Lozano, 2000, McIntyre et al., 2004], which operate at frequencies above 100 Hz. While our model does not satisfy the charge-balancing constraint required in the stimulation of *in vivo* systems, we believe that the present study improves our understanding of high-frequency neural oscillators.

## 2.5. The even-all multimodal transition

If the odd-all transition exists, is there a similar even-all or odd-even transition? In order to answer this question one should explore the vicinity of the even- $k$  regions of the response diagram. The ISI spectrum in Fig. 2.12 suggests that the answer to the question is likely to be affirmative. Here the even modes dominate, the lowest being  $k = 2$ . Around  $g_{syn} = 0.093\text{mS}/\text{cm}^2$  the mode locking is perfect with  $k = 4$ . Between 0.092 and  $0.093\text{mS}/\text{cm}^2$  the lowest odd modes are repelled, which is clearly seen in the case of  $k = 3$  and  $k = 5$ . Also between

0.093 and 0.094mS/cm<sup>2</sup> the dominant modes are  $k = 2, 4, 6$ , the ones with odd  $k$  occurring very seldom.

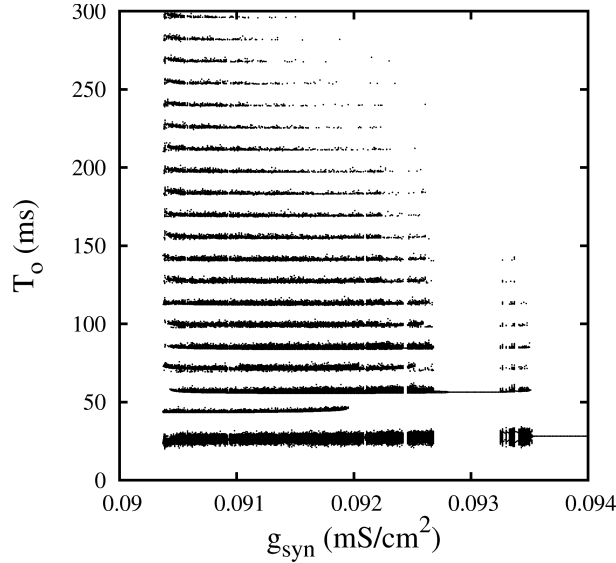


Figure 2.12: ISI as a function of the synaptic coupling at  $T_i = 14.1$ ms. Even modes dominate. The odd modes vanish at  $g_{syn} \approx 0.0927$ mS/cm<sup>2</sup>. For  $g_{syn} > 0.0927$ mS/cm<sup>2</sup> the relative frequency of occurrence of the odd modes is below 0.01.

Other regions where the even-all transition may occur is near the edges of the  $k = 2$  area of the  $T_i = 35$ ms and the  $T_i = 52$ ms resonances (see Fig. 3.4). In general any border between the even- $k$  state and the regime of irregular response is a candidate for such singular behavior. We will see in Chapter 3 that the competition between the odd and the even modes is one of the main features of the dynamics of the HH model.

Fig. 2.13 shows the transfer of weight between the odd and the even modes. The boundary between states of different parity is often extended and irregular, not sharp. In general we can expect to find the most complicated interplay of even and odd modes in the intermediate states between the states with small integer values of  $k$ . In the perithreshold regime near the main resonance the boundaries of  $k = \text{const}$  states have fractal character (see e.g. Fig. 3.9). This topic is expanded in Chapter 3.

Fig. 2.14 shows the weight of the lowest modes in the regime of irregular response at 13.85ms. At first only the modes  $k = 2$  and  $k = 4$  compete near  $k = 2$ . The weight of  $k = 4$  grows linearly at the expense of the  $k = 2$  state. As the synaptic coupling gets weaker, higher order modes, including the odd ones, come into play. Near the excitation threshold the ISI distribution has a

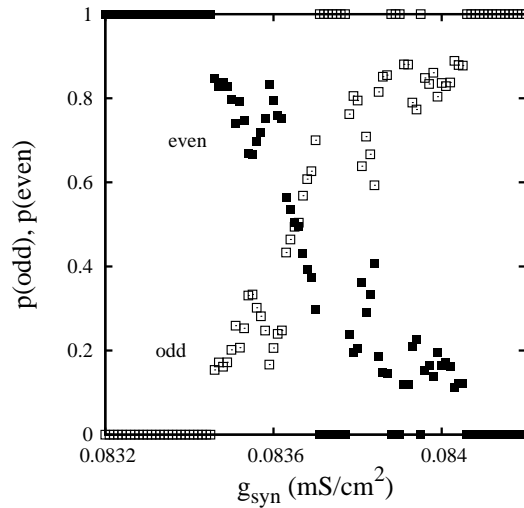


Figure 2.13: The change of the parity of the response between the odd-only (open squares) and even-only (filled squares)  $k$  at  $T_i = 16.1\text{ms}$ . This section was taken between the  $k = 3$  and  $k = 4$  states near the main resonance (see Fig. 3.3).

dual character. It consists of the states  $k = 2$  and  $k > 6$ , with the weight equally divided between the two parts.

One of the typical scenarios along the excitation threshold is the dominance of the lowest mode and the high order odd or even modes. Fig. 2.15 shows an example of such situation. Here the even modes dominate down to  $g_{syn} = 0.093\text{mS/cm}^2$ . The odd modes emerge below  $g_{syn} = 0.093\text{mS/cm}^2$ . Initially their relative weight  $p$  grows linearly, then faster than linearly, reaching a sharp maximum at  $g_{syn} \approx 0.092\text{mS/cm}^2$ , before falling off rapidly. The high-order even modes peak at  $g_{syn} > 0.092\text{mS/cm}^2$ , then almost disappear, and finally grow again. Near the threshold the weight of the  $k = 2$  mode remain close to 0.5.

This evolution of the relative frequencies of the different modes is shown in Fig. 2.16 (left). The ISI distribution in the perithreshold regime becomes bimodal (see Fig. 2.16 (right)). The bimodality of the ISI histogram implies high values of the coefficient of variation. In this example CV is of order 1.

For  $T_i$  in the vicinity of the main resonance of the HH model,  $T_{0res} \approx 17.5\text{ms}$ , and at larger  $k$  there is a quasi-linear crossover between the two parity regimes (see Fig. 2.13).

The change of parity of the response should be observable experimentally. On the border between two different  $k$  values a small change of the stimulus amplitude should drive the neuron through the transition. Some experiments in the similar parameter range as shown in Fig. 2.13 were performed earlier (see e.g. [Kaplan et al., 1996]), where the ISI histogram with the  $k = 4$  dominant mode was obtained.

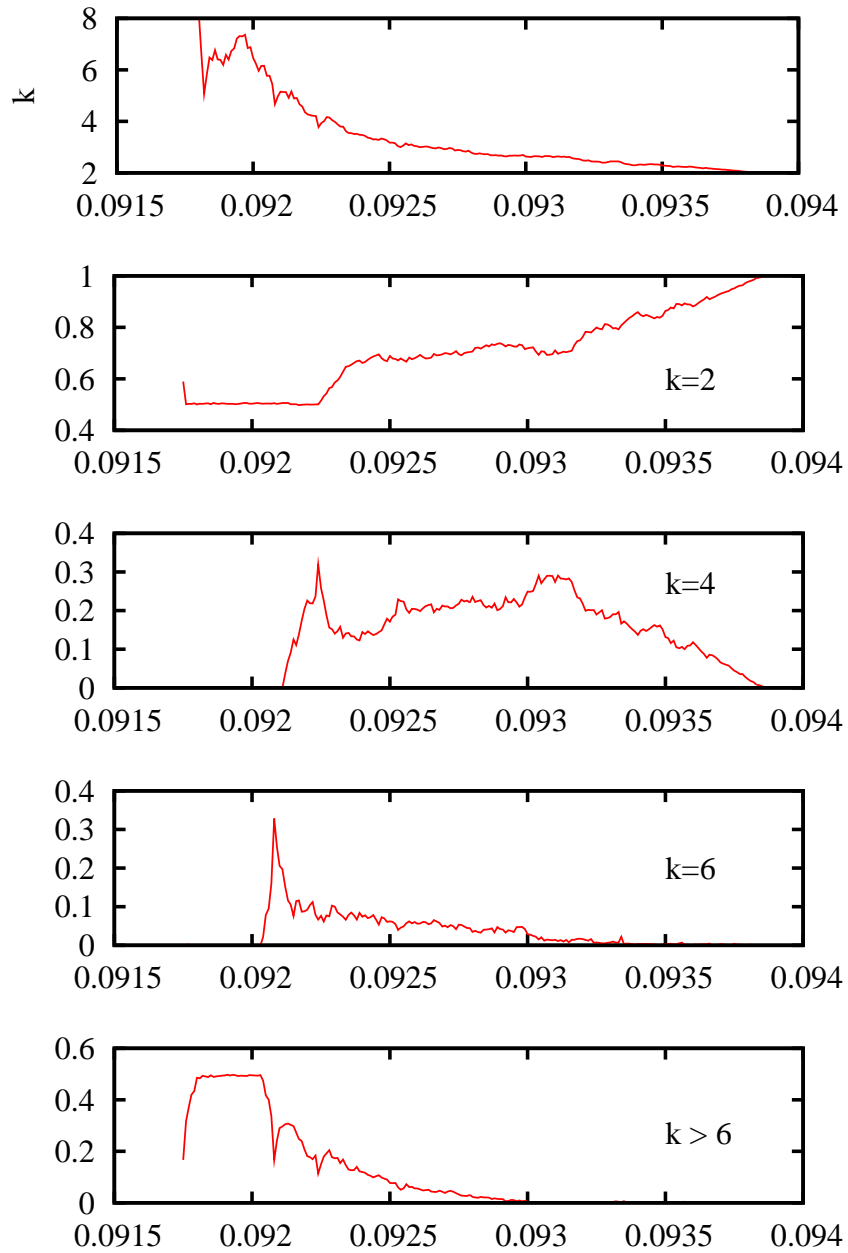


Figure 2.14: Spectrum of the lowest ISI modes in the irregular regime at  $T_i = 13.85\text{ms}$ . Note the dominance of the  $k = 2$  mode and the high-order modes near the excitation threshold.

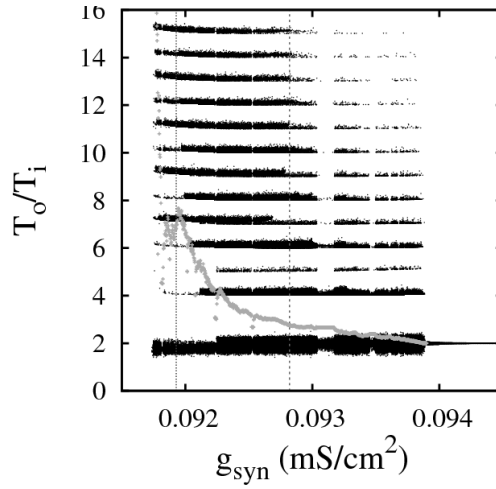


Figure 2.15: ISI near the excitation edge at  $T_i = 13.85\text{ms}$ . Grey points show the values of  $k$ . For  $g_{syn} > 0.0928\text{mS/cm}^2$  (right of the vertical dashed line) the odd modes almost do not occur (see also Fig. 2.16). Below  $g = 0.092\text{mS/cm}^2$  the high-order odd modes dominate over the high-order even modes (left of the dotted vertical line). The vanishing of the low-order even modes is marked by the local maximum of  $k$  slightly below  $g_{syn} = 0.092\text{mS/cm}^2$ .

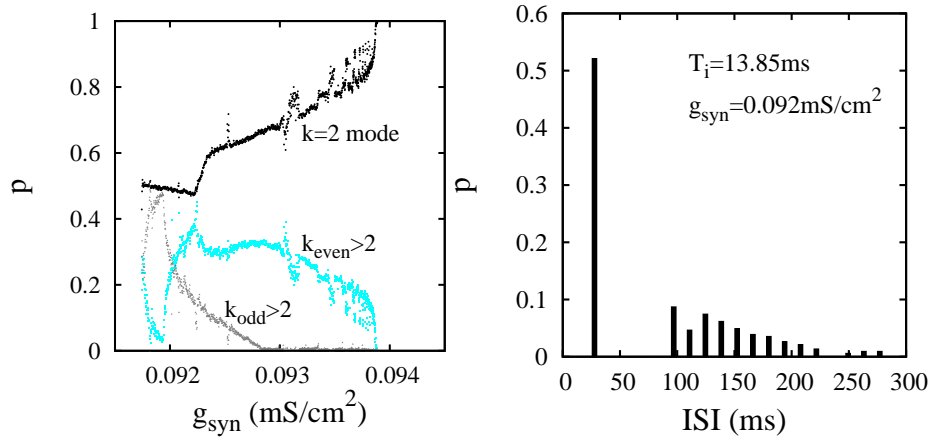


Figure 2.16: Left: The relative frequency of occurrence of the  $k = 2$  mode, the even modes with  $k > 2$  and the odd modes with  $k > 2$ , at  $T_i = 13.85\text{ms}$ . The competition between the odd and the even modes is seen most clearly near  $g_{syn} = 0.092\text{mS/cm}^2$ . Right: The relative frequency of occurrence of different modes at  $T_i = 13.85\text{ms}$  and  $g_{syn} = 0.092\text{mS/cm}^2$ . Note the absence of modes  $k = 3, 4, 5, 6$ .

## 3. Resonance

### 3.1. Introduction

The Hodgkin-Huxley neuron is primarily a type 2 neuron, responding with a firing rate of finite frequency when the stimulating current amplitude crosses a certain threshold. However in Chapter 2 we showed that this is not always true and the HH neuron may also have a continuous (or almost continuous) frequency-current amplitude curve. Although the HH neuron is the prototype for an entire class of conductance based models, its resonance structure has not been analyzed in sufficient detail.

In a widely studied HH model with a sinusoidal driving current there is one resonance at  $T_i = 17.5\text{ms}$ . Higher-order resonances are not seen. The response diagram for a sinusoidal current is a result of the two main features of the input signal: (i) continuously changing  $I(t)$ , which obscures the more subtle features of the neuron's dynamics, (ii) charge balancing, i.e. the time average of  $I(t)$  is 0.

The excitation threshold in presence of the sinusoidal current for  $T_i \gg T_{0res}$  depends linearly on  $T_i$ . This follows from the need to preserve the rate of increase of the driving current if the neuron is to spike. Otherwise the neuron will not fire. If  $T_i$  is increased e.g. twice, one has to increase the amplitude of  $I(t)$  by the same factor in order to excite the neuron. Thus for a sinusoidal current and  $T_i > T_{0res}$  the response diagram along the excitation edge is not really useful.

It is much more interesting to apply a current which is nonzero over only a fraction of the main resonance period  $T_{0res}$ , allowing the study of the neuron's intrinsic dynamics. This restriction reflects the refractoriness of the neuron. In the HH model the refractory period is of order 10 to 12ms. It is somewhat surprising that after many years of studying the HH model and its descendants there is no 'canonical' set of results showing response to perturbations of various functional forms, and the dynamics of even the basic model has not been not fully understood.

Since the existence of a resonance implies the presence of higher-order resonances it is important to find them. There are indications in the literature that the most interesting regime of the HH model lies in the vicinity of the excitation boundary [Clay, 2003]. This boundary itself need not be a smooth hypersurface separating a resting steady states from the excited state. We should therefore pay particular attention to the perithreshold regime. The HH neuron under a

periodic sequence of conductance pulses decaying exponentially was already defined in Chapter 2. We work with the same parameter set and the same driving current. Results presented in this Chapter were obtained from 30s-runs, discarding the initial 1s of data.

## 3.2. Results

A pulse input clearly shows the resonances of the HH neuron. The response diagram along the excitation threshold is shown in Fig. 3.1. The main resonance is located at  $T_i = T_{0res} = 17.5\text{ms}$ . The dominant mode at the resonance is  $k = 3$ . The next resonance at  $T_i = 35\text{ms}$  is dominated by the  $k = 2$  mode. Higher-order resonances are separated from the main resonances by multiples of  $T_{0res}$ . Each resonance contains regions of regular and irregular behavior (marked 'c' in Fig. 3.1). In the irregular regime the transition from the steady silent state to the excited one occurs via a period doubling bifurcation, see Fig. 3.2 (left). In bistable regions marked 'B' the firing and non-firing solutions coexist. The relevant bifurcation is shown in Fig. 3.2 (right). The type of solution obtained depends on the initial condition.

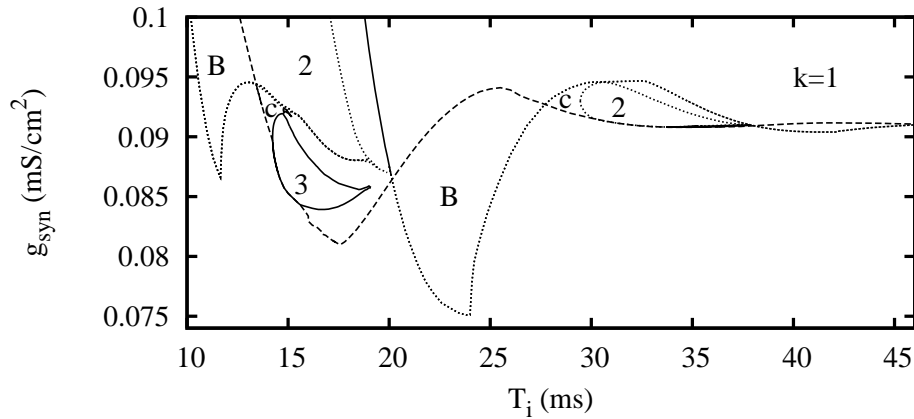


Figure 3.1: The response diagram along the excitation threshold. The main resonance is at  $T_i = 17.5\text{ms}$  and two higher-order resonances. Areas of bistable response are marked 'B'. Numbers indicate the value of  $k$  for each region. Regions of irregular response are marked 'c'.

A more detailed map of response is shown in Fig. 3.3. In the upper left corner of the diagram the neuron's firing is irregular, probably chaotic. The oval shapes are the competing modes  $k = 4$  and  $k = 5$ .

The dominant state of the main resonance is the  $k = 3$  mode marked by the large grey area in the center of Fig. 3.3. Near the tip of the resonance there is a sequence of mode-locked states separated by regions of irregular response (white areas). The values of  $k$  along the boundary of excitability are often high.

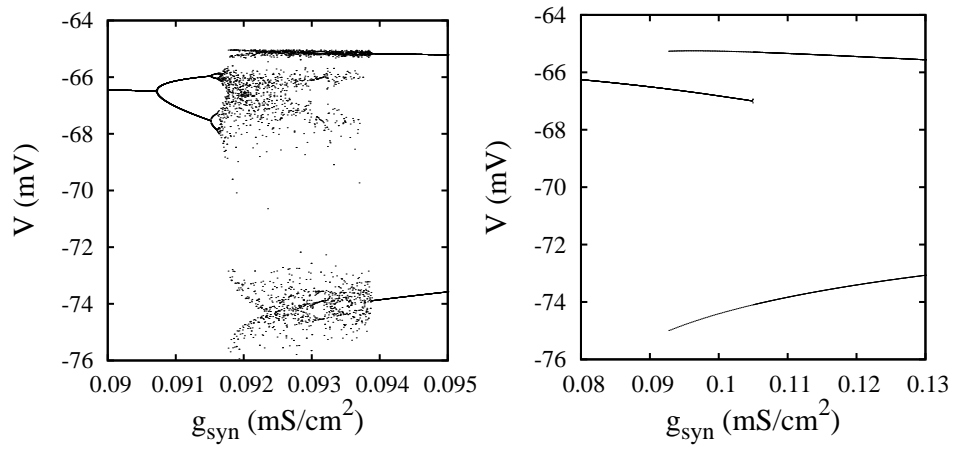


Figure 3.2: Left: Period doubling bifurcation between the silent state and the regime of irregular response at  $T_{in} = 13.85\text{ms}$ . Right: Below  $T_i = 13\text{ms}$  the bifurcation character changes. Here the silent state coexists with the excited state  $k = 2$ .

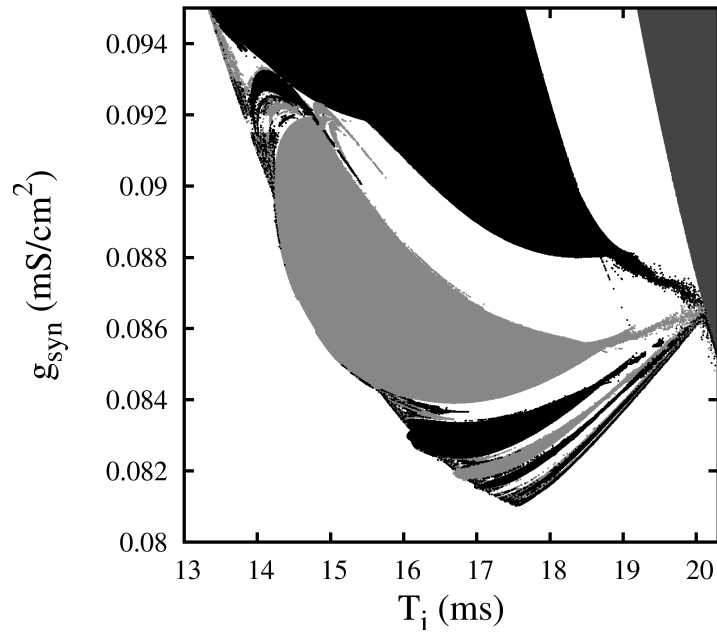


Figure 3.3: The map of the main resonance in the  $T_i$ - $g_{syn}$  plane. Black and light grey areas are the states with  $k$  even, odd respectively. Dark grey area on the right is the  $k = 1$  state. In the white areas between the states with integer  $k$  the entrainment ratio has noninteger values.

The resonant dynamics in Fig. 3.3 is a result of competition between the low-order fundamental mode and a combination of higher-order modes. The shape of the boundary itself is not smooth and depends on initial conditions, which confirms analysis of Ref. [Guckenheimer and Oliva, 2002].

The second-order resonance has a topological structure similar to the main resonance, see Fig. 3.4 (left). The pocket of irregular response occurs between the bistable regime and the dominant mode  $k = 2$ , where  $28\text{ms} < T_i < 30\text{ms}$ .

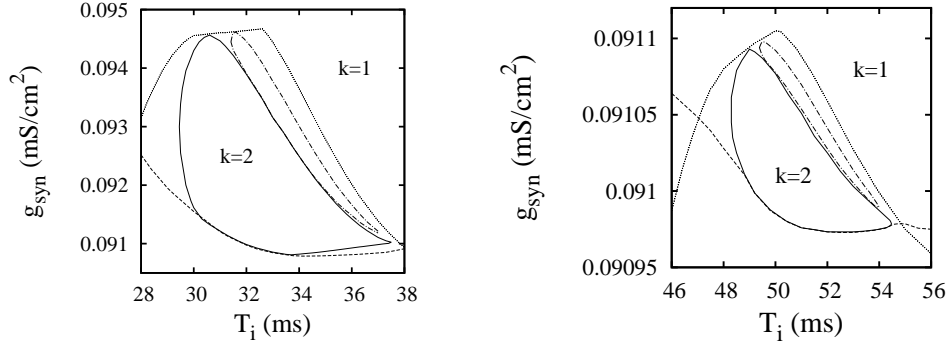


Figure 3.4: The topology of the resonant states at  $T_i = 35\text{ms}$  and  $T_i = 52\text{ms}$ . To the left of the  $k = 2$  state is the area of irregular response, which may be chaotic. States with fractional  $k$  appear between  $k = 1$  and  $k = 2$ .

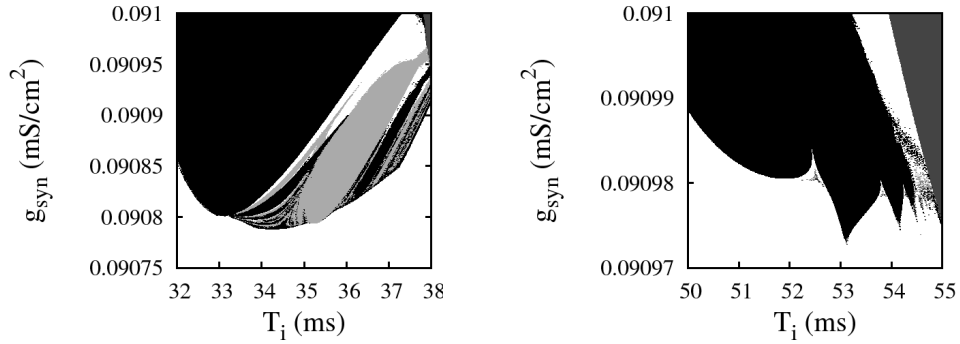


Figure 3.5: Details of the resonant states at  $T_i = 35\text{ms}$  and  $T_i = 52\text{ms}$  near excitation threshold. Black and light grey areas are the states with  $k$  even, odd respectively. Dark grey area is the  $k = 1$  state. White areas between states with integer  $k$  mark states with non-integer  $k$ .

The extent of the  $T_i = 52\text{ms}$  resonance along the  $g_{syn}$  axis is an order of magnitude smaller than the second-order resonance, see Fig. 3.4 (right). The areas occupied by each resonance decreases roughly exponentially with  $T_i$ . The fourth resonance was not seen in this calculation, although a slight anomaly of the excitation threshold was present near  $T = 69\text{ms}$ .

The details of the excitation boundary are shown in Fig. 3.5 (right). In this case the boundary at the tip has the form of sharp Arnold tongues with  $k = 2$ . The physical origin of these features is not clear at the moment. They are not seen in the other two resonances. States with  $k > 2$  appear irregularly in few spots along the excitation threshold.

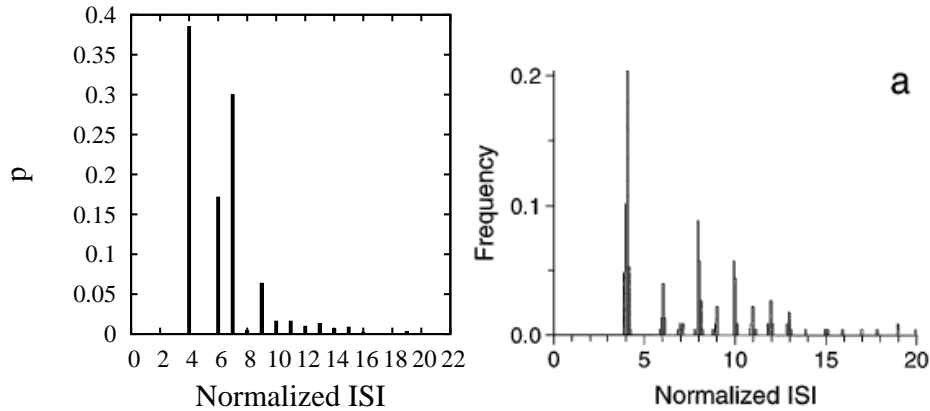


Figure 3.6: Left: The interspike interval histogram for  $T_i = 16\text{ms}$  and  $g_{syn} = 0.0836\text{mS}/\text{cm}^2$ . Note the absence of the mode  $k = 5$ . Right: The experimental data from Fig. 4a of Ref. [Kaplan et al., 1996] obtained at  $T_i = 12.2\text{ms}$  for rectangular current pulses of width 1ms and amplitude 0.6mA. Figure reprinted with permission from D. T. Kaplan, J. R. Clay, T. Manning, L. Glass, M. R. Guevara, and A. Shrier, *Physical Review E* **76**, 4074 (1996). Copyright 1996 by the American Physical Society.

In the resonant regime close to the excitation boundary the lower order modes are absent. An example of an ISI histogram in this limit is shown in Fig. 3.6 (left). Similar results were obtained experimentally in a study of a response of the squid giant axon to a periodic train of rectangular current pulses of width 1ms and amplitude 0.6mA [Kaplan et al., 1996] (see Fig. 3.6, right). In the experimental data taken at  $T_i = 12.2\text{ms}$  the lowest mode is  $k = 4$ . Mode  $k = 5$  is absent. Among the modes  $k > 5$  the even modes clearly dominate. Although the relative frequency of occurrence of the modes  $k > 6$  is not reproduced in Fig. 3.6, the dominance of the  $k = 4$  and the absence of the  $k = 5$  mode agree with experiment. We also know from Chapter 2 that it is easy to obtain an ISI distribution such that either odd or even modes dominate. The comparison of Fig. 3.6 to experimental data and simulation using the FitzHugh-Nagumo model with short rectangular current pulses [Kaplan et al., 1996], suggests that the main features of the neuron response do not depend significantly on the precise form of an individual pulse, when the pulse width is much smaller than the resonance time scale.

It would be useful to explore experimentally the resonance regime in more detail in order to map the synchronized states and areas of irregular response. In our calculation the mode-locked and irregular states alternate along the exci-

tation edge. We expect the relative alignment of these states to be reproduced in experiment. The exact position of the tip of the experimentally found resonance may occur at  $T_i$  being 2 to 4ms smaller than in the present calculation. This statement follows from the comparison of our results to the measurements of Refs. [Takahashi et al., 1990] and [Kaplan et al., 1996].

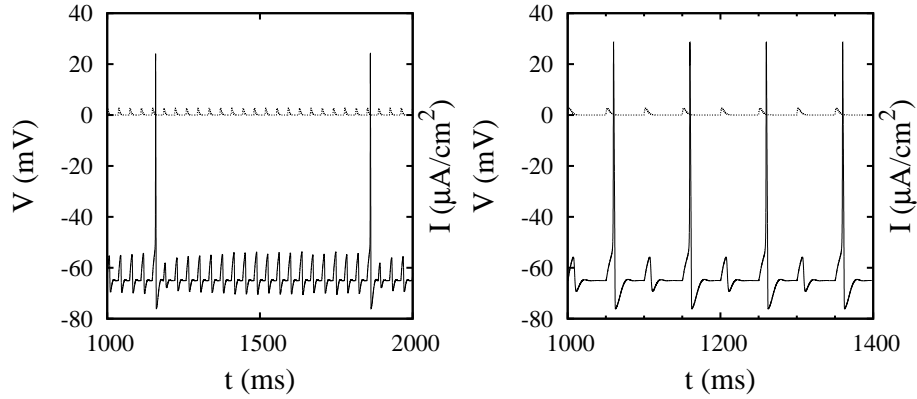


Figure 3.7: Sample spike trains at  $T_i = 37\text{ms}$  and  $g_{syn} = 0.0908415\text{mS}/\text{cm}^2$  (left),  $T_i = 50\text{ms}$  and  $g_{syn} = 0.091\text{mS}/\text{cm}^2$  (right). The synaptic current is drawn with the dotted line.

Fig. 3.7 shows two sample spike trains. The first one, obtained at  $T_i = 37\text{ms}$ , very close to the silent state, is the  $k = 19$  state. The output frequency is 19 times smaller than the stimulus frequency. This result supports some of the conclusions drawn by Clay [Clay, 2003], who observed the continuous slowing down of the response near the firing threshold. The firing rate is a continuous function of the stimulus amplitude in many parts of the perithreshold regime. Therefore the classification of the HH neuron as class 2 neuron is not exactly correct. Another experimental detail confirmed by our calculations is the appearance of the  $k = 3$  mode near  $T_i = 17\text{ms}$  [Kaplan et al., 1996]. Those results also confirm our analysis of the interplay between the odd and even modes in Chapter 2 of this work.

The dynamics near the tip of the resonance deserves further scrutiny. In order to eliminate the influence of exponential tails of the stimulus chosen in Chapter 2, we replace the time dependence  $(t/\tau)e^{-t/\tau}\Theta(t)$  in Eqn. 2.12 with  $[1 - (1 - t/\tau)^2]\Theta(t)\Theta(2\tau - t)$  and calculate ISI at  $T_i = 18\text{ms}$ . Fig. 3.8 shows the logarithmic plot of the ISI as a function of the difference  $g_{syn} - g_c$ , where  $g_c$  is an approximate location of the excitation threshold. Both the lower and upper ISI envelope scale with exponent  $-1/2$ . Values of  $T_o$  near the upper edge do not make significant contribution and the average ISI follows closely the lower edge of this distribution. This means that close to the excitation boundary the ISI histogram is weakly bimodal, i.e. its second peak is small.

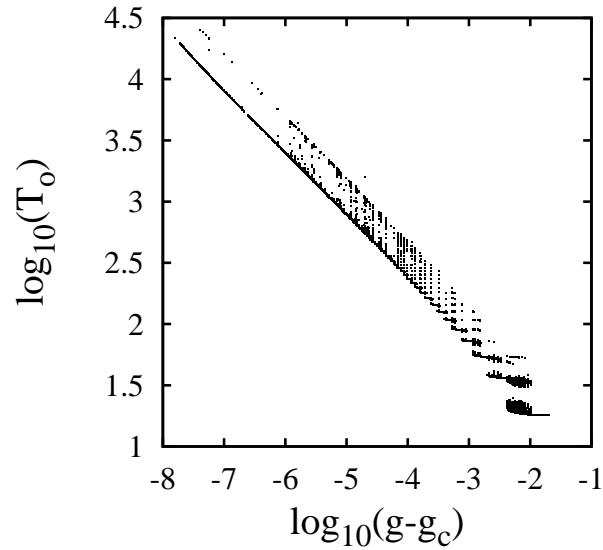


Figure 3.8: Scaling of the output ISI near the tip of the resonance, at  $T_i = 18\text{ms}$ , for a spike train input in which the time dependence of each pulse is  $[1 - (1 - t/\tau)^2]$  for  $0 < t < 2\tau$ .

It is clear now that the HH neuron is capable of responding with very low frequencies not only in the anti-resonance regime (see Chapter 2) but also in the resonance limit.

Fig. 3.9 shows an enlargement of a small patch of the main resonance between the  $k = 2$  and  $k = 3$  states. The boundary between these states has a fractal character, resulting from the competition of even and odd ISI modes. The areas with  $k = 2$  are marked black. Light grey are states  $k = 3$ . There are small patches of  $k = 4$  marked dark grey in the lower left part of the figure. The rest are the states with fractional  $k$ .

Guckenheimer and Oliva showed that the boundary between the stable rest state and periodically firing state is a fractal set. We have shown that this is true also for the boundaries between different mode-locked states, where modes of different parity compete.

We have found relatively large regions of the parameter space near the excitation threshold where irregular (probably chaotic) solutions exist. The irregularity in the HH model arises from the competition of different response modes. In the resonance regime the transition between neighboring mode-locked states frequently occurs through excitation of at least several higher order modes. This is reminiscent of the multimodal transition from Chapter 2. We may conclude that the mode parity is an important factor also in the resonant regime. For example near the  $k = 2$  region there is a tendency for the low order even modes to dominate. Similar phenomenon occurs with odd modes near the  $k = 3$  area.



Figure 3.9: Section of the phase diagram between  $T_i = 14.9\text{ms}$  and  $T_i = 15.2\text{ms}$ ,  $g_{syn} = 0.091\text{mS/cm}^2$  and  $g_{syn} = 0.0919\text{mS/cm}^2$ .

### 3.3. The quasi-discrete return map

The ISI return map in Fig. 3.10 shows the ISI modes available in the irregular regime at  $T_i = 14.25\text{ms}$ . Although the response is irregular, the number of modes taking part in the response is not very large and the spread of possible ISI values within each band is very small, i.e. we have a quasi-discrete spectrum of intervals.

We can enumerate all the possible transitions between subsequent modes:

- 2  $\rightarrow$  3, 4, 5 or 7
- 3  $\rightarrow$  2, 3, 4, 5, 6 or 7
- 4  $\rightarrow$  3 or 5
- 5  $\rightarrow$  2, 3 or 5
- 6  $\rightarrow$  3
- 7  $\rightarrow$  5

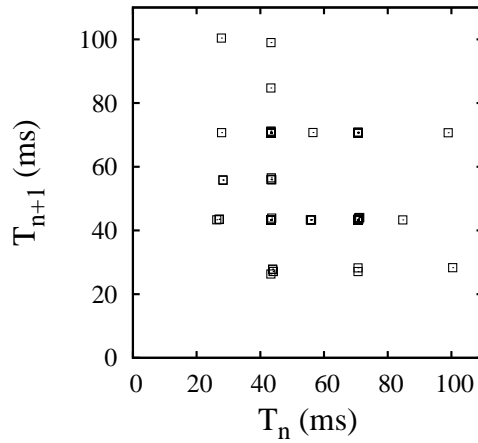


Figure 3.10: The return map at  $T_{in} = 14.25\text{ms}$  and  $g_{syn} = 0.0915\text{mS}/\text{cm}^2$ . This state exists between the  $k = 2$  mode and the excitation threshold.

For example mode 2 may be followed by mode 3, 4, 5 or 7. There is no symmetry of transitions between various modes. For example: mode 7 cannot be followed by mode 3, although mode 7 may follow mode 3; mode 2 may be followed by mode 4, but the opposite is not true; mode 4 may be followed by mode 5, but 5 is not followed by 4. The dominant mode  $k = 3$  has the most connections. It can be followed by any of the other intervals. We can enumerate also all the possible cycles, although it should be verified numerically, whether all of them are realized, including their relative frequency of occurrence. Here are some examples of shorter cycles:

$2,3, l = 5$   
 $2,4,3, l = 9$   
 $2,4,5, l = 11$   
 $2,5, l = 7$   
 $2,5,3, l = 10$   
 $2,7,5, l = 14$   
 $3,2, l = 5$   
 $3, l = 3$   
 $3,4, l = 7$   
 $3,5, l = 8$   
 $3,6, l = 9$   
 $3,7,5, l = 15$   
 $4,5,2, l = 11$   
 $4,5,3, l = 12$

Here  $l$  is the length of the minimum cycle. The longest minimum cycles are associated with mode 7, which communicates with the lowest two modes, 2 and 3, only indirectly through mode 5. We can infer from Fig. 2.14, which shows the weight transfer between modes, that the degree of participation of different cycles in the dynamics is a continuous or nearly continuous function of the independent parameter.

The entire dynamics of the neuron with this quasi-discrete return map may be viewed as an irregular sequence of integer numbers. There are some attempts in the literature [Kocarev and Szczepanski, 2004, Kocarev et al., 2006] to define and study properties of discrete chaotic systems, using the notion of pseudo-chaos in discrete spaces [Kocarev and Szczepanski, 2004]. While the ISI spectrum of the HH model is not exactly discrete, it offers an intriguing possibility of studying chaos in an almost discrete space.

It may be useful to study the evolution of the return map as the system approaches the excitation boundary. In this limit the ISI distribution has a bimodal character, provided  $T_i$  is not too close to the resonance  $T_{0res}$ . Since the intermediate modes gradually disappear we would expect to see a sequence of transitions towards higher values of  $T_o$ . The nature of these transitions and their dependence on the model parameters may be among the basic properties of resonant neurons.

## 4. Noise

### 4.1. Introduction

Noise in neural cells may come from three sources [Lecar and Nossal, 1971a,b, White et al., 1998, 2000, Manwani and Koch, 1999a,b, 2001, Faisal et al., 2008]: (a) thermal noise arising from the membrane resistance (Johnson noise), (b) random background synaptic activity, (c) stochastic channel openings and closings.

The thermal noise, coming from a large ensemble of independent sources, has almost flat power spectral density and its amplitude can be well approximated by the Gaussian distribution. Its power spectral density in equilibrium is given by  $S = 2k_B TR$ , where  $T$  is the temperature and  $R$  is the resistance of the sample.

The background synaptic activity is typically modeled as a homogenous Poisson process. Assuming presynaptic spikes to have the form of the  $\delta$ -function and small synaptic current for a unitary synaptic event, we have  $I_{syn}(t) = g_{syn}(t)(V - E_{syn})$ . Using the Campbell's theorem, the average  $I_{syn}$  and variance can be calculated in the following way,

$$\langle I_{syn}(t) \rangle_t = \lambda(V - E_{syn}) \int_0^\infty g_{syn}(t) dt, \quad (4.1)$$

$$\sigma^2 = \lambda(V - E_{syn})^2 \int_0^\infty [g_{syn}(t)]^2 dt, \quad (4.2)$$

where  $\lambda$  is the input rate. The channel noise results from the the randomness of opening and closing of individual channels. Details depend on the particular kinetic scheme chosen to represent transitions between the various states of the channel.

Our model consists of the same components as before,

$$C \frac{dV}{dt} = -I_{Na} - I_K - I_L - I_{syn}. \quad (4.3)$$

Here the currents have the usual meaning. The synaptic current is now taken as a sum of a periodic and a stochastic term,

$$I_{syn}(t) = g_{syn} \sum_n \alpha(t - t_{in})(V_a - V_{syn}) + D\xi(t), \quad (4.4)$$

where the time dependence of the conductance pulse is given by Eqn. (2.12). The fluctuating current is approximated as a Gaussian white noise,

$$\langle \xi_i(t) \rangle = 0, \quad \langle \xi(t)\xi(t') \rangle = 2D\delta(t - t'). \quad (4.5)$$

The equations are integrated using the second-order stochastic Runge-Kutta algorithm [Honeycutt, 1992]. The time step is  $dt = 0.01\text{ms}$ .

## 4.2. Sensitivity of the firing rate to noise

The phenomenon of increased sensitivity to small perturbations at a preferable intensity of noise is known as stochastic resonance (SR) [McNamara and Wiesenfeld, 1989, Longtin, 1993, Douglass et al., 1993, Wiesenfeld and Moss, 1995, Levin and Miller, 1996, Gammaitoni et al., 1998]. Usually it is characterized as a maximum of the power spectral density as a function of  $D$ . In excitable systems noise has the largest effect close to the excitation boundary, e.g. allowing detection of subthreshold signals.

In an excitable oscillator driven by noise with no periodic component the most regular response is obtained at some intermediate noise intensity. This phenomenon is related to SR and is known as coherence resonance (CR) [Pikovsky and Kurths, 1997].

We will show the dependence of the neuron's response frequency on the stimulus amplitude, its frequency and intensity of noise. Figs. 4.1-4.2 shows the vanishing of mode-locked plateaus with increasing noise at the main resonance,  $T_i = 17\text{ms}$ . The flat areas of  $k$  vs.  $g_{syn}$  decrease at a similar rate on both ends of the plateau. At the value of  $D$ , when the entire plateau just disappeared, the  $k - g$  curve crosses the center of the plateau. For points on the plateau below the midpoint the response frequency decreases as a function of  $D$ , reaches maximum, and then increases towards  $f_o = 1000/T_{0res}$ . In the limit of large noise,  $f_o$  gradually becomes almost independent of  $g_{syn}$ .

In the presence of noise the plateaus of constant  $k$  are reduced and disappear with increasing  $D$ , see Figs 4.1. This means that at constant  $T_i$  the neuron becomes more sensitive to changes of the synaptic conductivity. For larger  $g_{syn}$ ,  $k$  is smaller and the frequency of the input signal is lowered by a smaller factor. A neural network built with such neurons is capable of detecting small alterations of  $g_{syn}$ . The sensitivity grows with the number of neurons the signal passes through. However this statement is valid only in an average sense. The expectation value of the output frequency was obtained from 100 independent simulation runs of over 30 s each.

In Fig. 4.3  $D$  is varied between 0.1 and 10 at the resonance  $T_i = 17\text{ms}$ , for two values of  $g_{syn}$  near the threshold. The output frequency,  $f_o = f_i/k$ , is more affected by noise when  $g_{syn} = 0.08\text{mS/cm}^2$ , which is just below the  $D = 0$  threshold of  $0.082\text{mS/cm}^2$ .

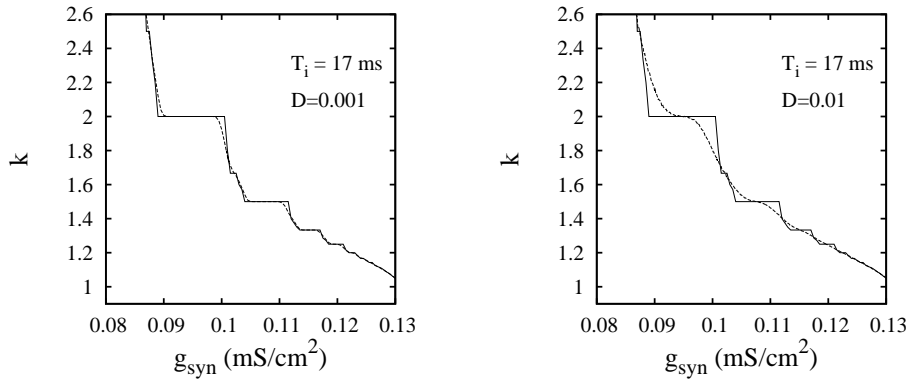


Figure 4.1: The dependence of  $k$  on  $g_{syn}$  for  $D = 0.001$  (left),  $D = 0.01$  (right). Here  $T_i = 17$ ms.

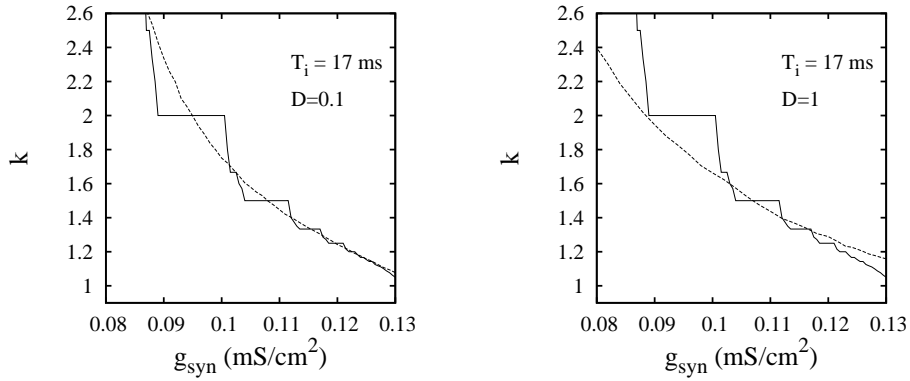


Figure 4.2: The dependence of  $k$  on  $g_{syn}$  for  $D = 0.1$  (left),  $D = 1$  (right). Here  $T_i = 17$ ms.

In the interval between  $T_i = 1$  and 10ms in Fig. 4.4,  $k$  is infinite. Increasing noise lowers the excitation threshold but the anti-resonance is still clearly seen (see Fig. 4.5, left).

In the limit of large noise  $k$  becomes independent of  $g_{syn}$  (see Fig. 4.5, right),  $k \rightarrow T_{0res}/T_i$ , where  $T_{0res}$  is the scale of the main resonance. For  $T_i > T_{0res}$  the average output firing rate is greater than the input rate. Noise has the effect of transforming the input frequencies toward the preferred, resonance frequency  $T_{0res}$ .

The effect of noise at  $g_{syn} = 0.25$ mS/cm<sup>2</sup>, which is more than twice the typical threshold level, is shown in Fig. 4.6. The mode-locked regions are here the lines of constant slope. An important feature is the initial fall of the output frequency  $\bar{f}_o$  at high  $f_i$ , when  $D$  increases from 0 to 0.05, before increasing again for larger  $D$ . This is a manifestation of a stochastic anti-resonance, which is the subject of the Section 4.3.

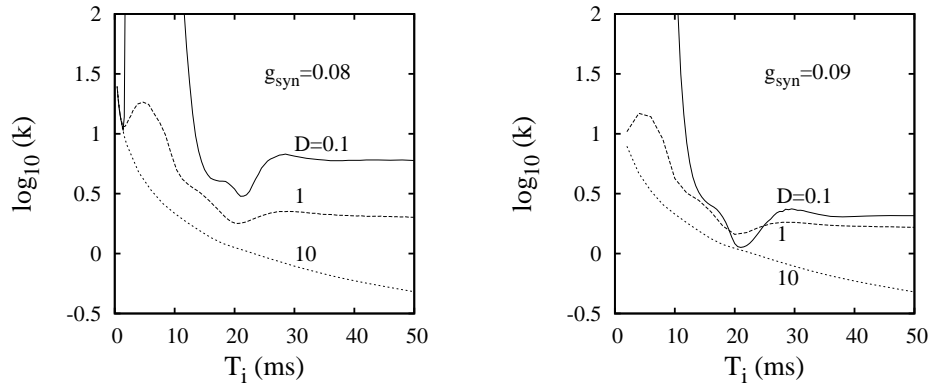


Figure 4.3: The dependence of  $k$  on  $T_i$  and noise intensity for  $g_{syn} = 0.08\text{mS}/\text{cm}^2$  (left),  $g_{syn} = 0.09\text{mS}/\text{cm}^2$  (right). The resonance is more pronounced at the smallest noise,  $D = 0.1$  (solid line), near the excitation threshold.

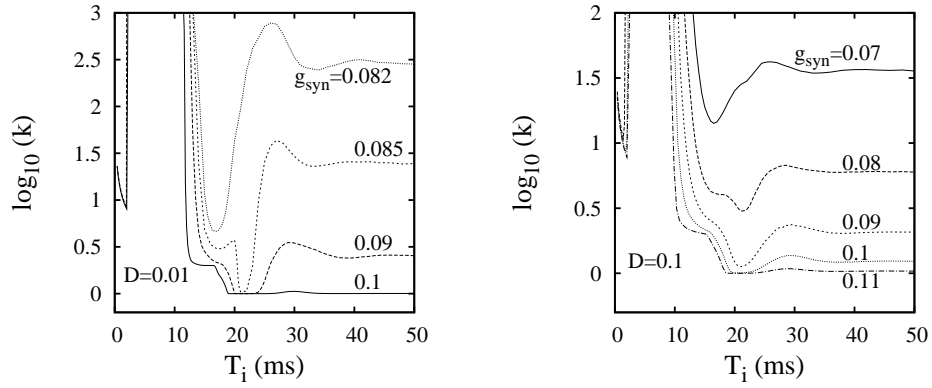


Figure 4.4: The dependence of  $k$  on  $T_i$  for different  $g_{syn}$  and  $D = 0.01$  (left),  $D = 0.1$  (right). The minima of the  $g_{syn} = 0.082\text{mS}/\text{cm}^2$  curve coincide with the minima of the deterministic resonance.

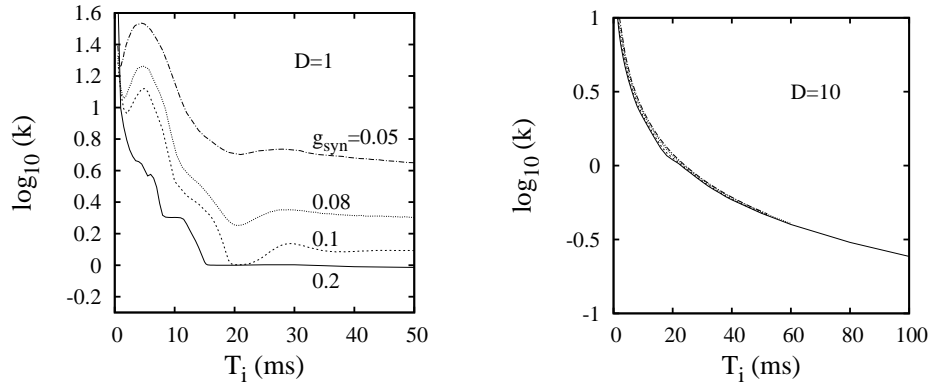


Figure 4.5: The dependence of  $k$  on  $T_i$  for different  $g_{syn}$  and  $D = 1$  (left),  $D = 10$  (right). For large  $D$ ,  $k \rightarrow T_{0res}/T_i$ .

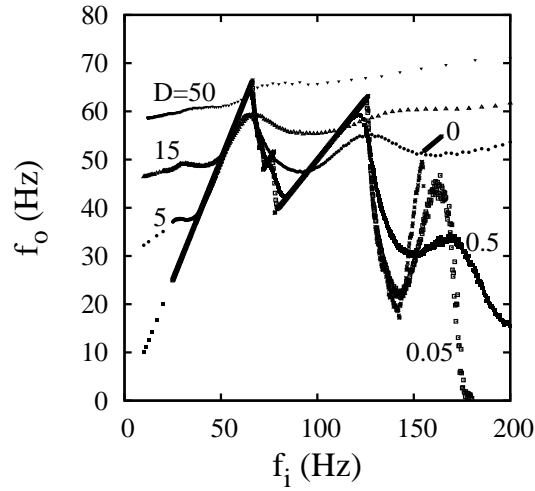


Figure 4.6: The relation between the input frequency  $f_i$  and the average output frequency  $\bar{f}_o$  for  $g_{syn} = 0.25\text{mS}/\text{cm}^2$  and different noise levels.

Fig. 4.7 shows  $k = \bar{T}_o/T_i$  in the limit  $g_{syn} = 0$  at the resonance  $T_i = 17.5\text{ms}$ . The addition of noise makes the exponential tail of  $k$  vs.  $g_{syn}$  dependence extend to  $g_{syn} = 0$ . In other words, the excitation threshold is driven to 0.

There is a resonance at a very short time scale, of order  $0.1\text{ms}$ . However its origin is unclear at present and it would require further study to understand its properties.

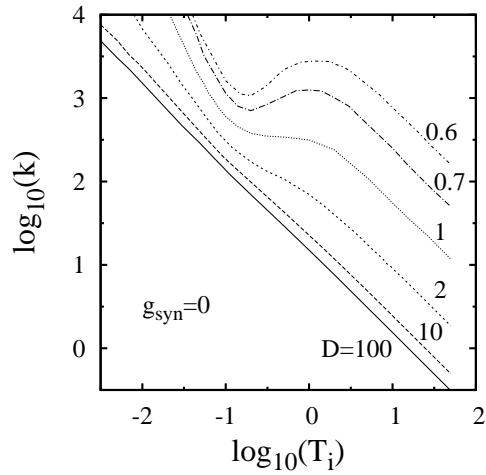


Figure 4.7: The value of  $k$  as a function of the input interspike separation in the limit of vanishing synaptic coupling. There is a resonance at  $T_i \sim 0.1\text{mS}/\text{cm}^2$ .

### 4.3. Stochastic anti-resonance

Cortical cells of mammals *in vivo* respond with high variability even to repeated presentations of identical stimuli [Harsch and Robinson, 2000]. The reaction of the same cells *in vitro* to a fluctuating input is reproducible and quite precise [Mainen and Sejnowski, 1995, Nowak et al., 1997, Harsch and Robinson, 2000]. Our aim is to compare the firing variability resulting from noise to the variability due to the internal deterministic nonlinearity of the neuron.

Fig. 4.8 shows the coefficient of variation of the output ISI as a function of the noise intensity for different synaptic firing rates. The synaptic conductance density is fixed at  $g = 0.25\text{mS}/\text{cm}^2$ . The maximum CV occurs at the anti-resonances, at 7ms, 14ms and 40ms.

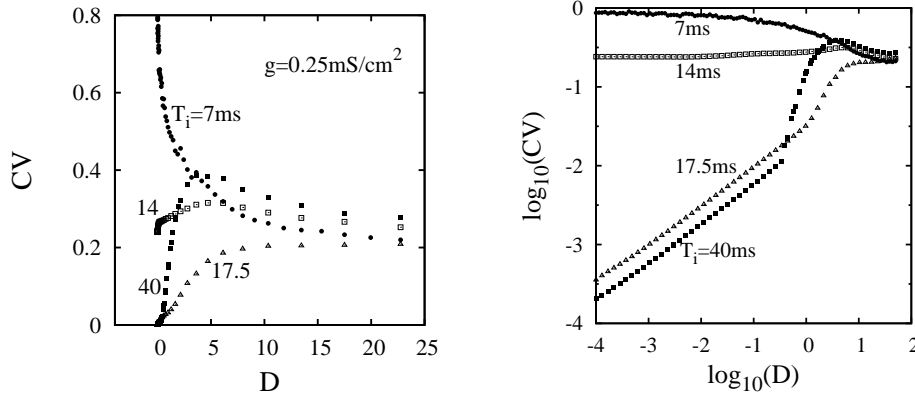


Figure 4.8: The coefficient of variation as a function of the noise intensity for  $g_{syn} = 0.25\text{mS}/\text{cm}^2$  and several values of the input period  $T_i$ . Left: linear scale, right: logarithmic scale.

Fig. 4.8 shows the CV as a function of the noise intensity at different  $T_i$ . The  $T_i = 17.5\text{ms}$  curve rises monotonically from 0 and saturates slightly above 0.2. The curves for  $T_i = 14\text{ms}$  and  $T_i = 40\text{ms}$  rise more steeply and have a maximum of order 0.3 – 0.4 near  $D = 5$ . The behavior at  $T = 14\text{ms}$  and  $T = 40\text{ms}$  may be called an anti-resonance, since the highest uncertainty of output ISI occurs at an intermediate noise level.

This phenomenon is opposite to coherence resonance and stochastic resonance, where the presence of noise increases the signal to noise ratio (SNR) and allows the system to respond with higher precision. The optimum SNR occurs at some intermediate  $D$ . The maximum of the CV as function of the average noise amplitude is a clear demonstration of a stochastic anti-resonance. This phenomenon was recently noticed theoretically [Gutkin et al., 2008, 2009] and experimentally [Paydarfar et al., 2006, Sim and Forger, 2007]. The noise may lower the neuronal activity or even turn it off. This may happen in the modes with the high value of  $k$  whose trajectories are close to the stable rest state. The

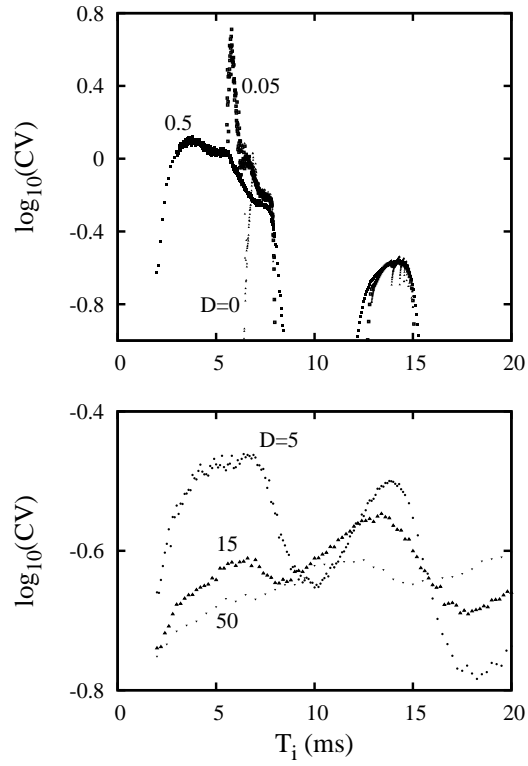


Figure 4.9: The coefficient of variation of the output ISI as a function of  $T_i$  at  $g_{syn} = 0.25\text{mS}/\text{cm}^2$  as a function of  $T_i$  for small noise intensity (left) and large noise intensity (right).

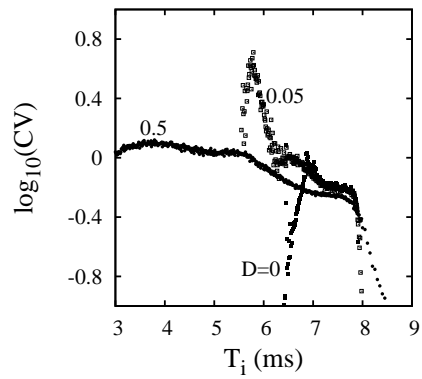


Figure 4.10: Expanded view of the main anti-resonance from Fig. 4.9. At  $D = 0.05$  the peak values of the CV are several times larger than those at  $D = 0$  and  $D = 0.5$ .

noise can then shift the trajectory from the basin of attraction of a stable limit cycle to the stable rest state.

The analysis of the multimodal transition in Chapter 2 shows that the origin of this effect lies in the multimodal behavior of the system. More precisely it is the competition between the odd and the even ISI modes that leads to a singular dependence of the CV on  $T_i$  and  $g_{syn}$  in a deterministic HH model. As can be seen in Fig. 4.8, for  $T_i$  near 7ms the maximum CV is of order 1 and lies very close to  $D = 0$ . The CV has a cusp singularity at the multimodal odd-all transition, see Fig. 2.8 in Chapter 3. This anti-resonance is most pronounced in the vicinity of this transition. In Fig. 4.9 (left) the peak CV value is several times larger for  $D = 0.05$  compared to the maxima for  $D = 0$  and  $D = 0.5$ .

#### 4.4. Scaling near the edges of the mode-locked states

Engelbrecht and Mirollo [Engelbrecht and Mirollo, 2009] showed that periodically driven 1D neurons exhibit scaling at the edges of the mode-locked plateaus. Plateaus are characterized by the fixed points of the map

$$F^q(t) = t + pT_i, \quad (4.6)$$

where  $p$  and  $q$  are integer,  $k = p/q$ . The scaling quantity is the average deviation from entrainment,  $|\bar{T}_o - kT_i|$ , which is analogous to the disorder parameter in phase transitions. In the integrate-and-fire (IF) model studied by the authors of Ref. [Engelbrecht and Mirollo, 2009] all left edge plateaus are characterized by continuous  $F$ . The scaling exponent is then  $\beta = 1/2$ . Near the right edges, the scaling is logarithmic,

$$|\bar{T}_o - kT_i| \sim \frac{-1}{\log |g - g_c|}. \quad (4.7)$$

Their 1D analysis is also applicable to higher dimensional models, such as the Connor-Stevens model [Connor and Stevens, 1971] in 7-dimensional parameter space, since the underlying dynamics of this and other models using dynamical gating variables is essentially one-dimensional.

Our results for the HH model partially support their conjecture, (see Fig. 4.11, left), where the scaling exponent is clearly  $1/2$ . All left bifurcations in the model studied here are continuous and all right-edge bifurcations are discontinuous. This is different from the IF model [Engelbrecht and Mirollo, 2009], where some of the bifurcations at the right edge are tangent, e.g. at  $k = 3/2, 7/5$ , and  $11/8$ . The discrepancy can probably be explained by investigating the role played by the magnitude of the synaptic drive. As suggested in Ref. [Engelbrecht and Mirollo, 2009], all right-edge bifurcations are continuous if the constant component of the current is below some threshold and the oscillatory drive is sufficiently small. Decomposing the synaptic current in Eqn. (2.11) into  $I_{ave} = \langle I_{syn}(t) \rangle_t$  and oscillatory part, one might study the effect of the relative size of the two components on the dynamics near the right edges of the mode-locked plateaus.

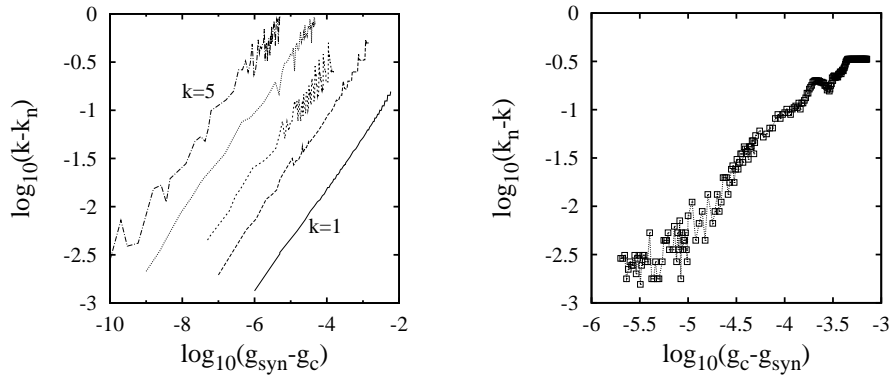


Figure 4.11: Left: Deviation from the perfect mode locking at the left edge of a  $k = k_n = \text{const}$  plateau as a function of  $g_{syn} - g_c$ . The curves, from right to left, represent  $k_n = 1, 2, 3, 4, 5$ , respectively. In each case the deviations from the straight line gradually disappear when averaging over long times. The scaling exponent is  $1/2$ . Right: At the right edge of the  $k = 2$  mode-locked plateau the scaling seems to be linear although this conclusion is not firm. In both diagrams  $T_i = 17\text{ms}$ ,  $D = 0$ .

In the presence of small noise the scaling at the right edges of the plateaus becomes linear. Noise regularizes the response and affects scaling at the dynamic transition points.

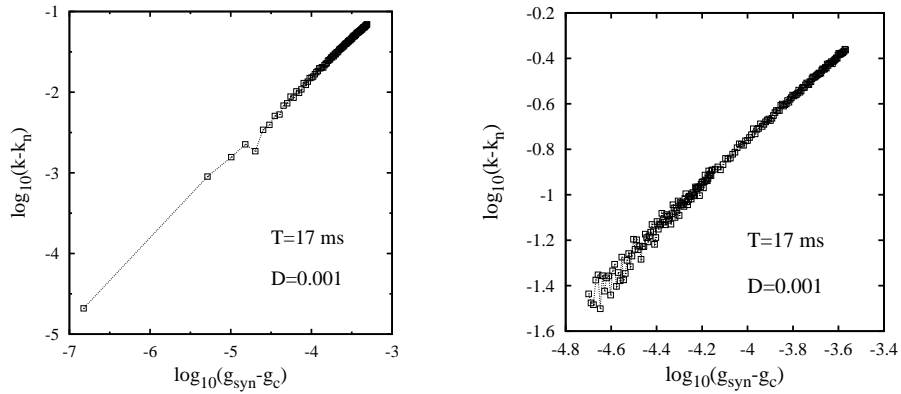


Figure 4.12: The linear scaling of the deviation from entrainment at the right edge of a mode-locked plateau in the presence of small noise for  $k_n = 9/5$ ,  $T_i = 17\text{ms}$ ,  $D = 0.001$  (left),  $k_n = 5$ ,  $T_i = 17\text{ms}$ ,  $D = 0.001$  (right).

Fig. 4.12 shows results for the plateaus  $k_n = 9/5$  and  $k_n = 5$ . Fig. 4.13 presents a detailed view of the transition at the right edge of the  $k = 2$  plateau with  $T_i = 17\text{ms}$ . The transition occurs at  $g_{syn} = 0.1008\text{mS}/\text{cm}^2$ .

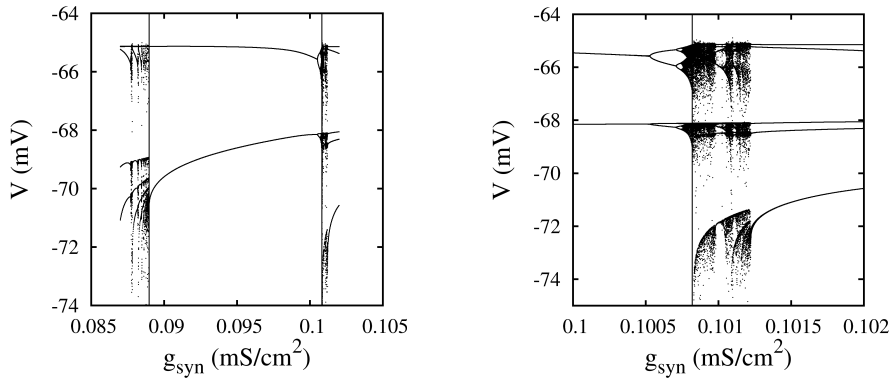


Figure 4.13: Left: The bifurcation diagram of the  $k = 2$  plateau at  $T_i = 17\text{ms}$ . The vertical lines mark the edges of the mode-locked region. Right: More detailed view of the bifurcation at the right edge of the plateau. The right plateau edge is located at  $g_{syn} = 0.1008\text{mS/cm}^2$ .

In order to better understand what happens at the transition, we plot the output spike train at  $g_{syn} = 0.1007\text{mS/cm}^2$ , within the plateau, and at  $g_{syn} = 0.1009\text{mS/cm}^2$ , which is just outside the edge, see Figs. 4.13 and 4.14. In Fig. 4.14 (right) there is one additional spike compared to Fig. 4.14 (left) and the mode-locking is not perfect. However, away from the additional spike the regularity is still preserved in the local sense. The perturbation caused by the breaking of the perfect locking is local, affecting only the preceding and the following ISI.

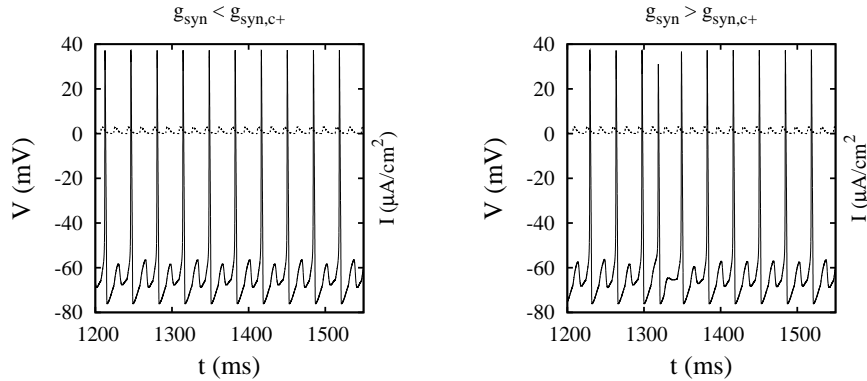


Figure 4.14: The spike train near the right edge of the  $k = 2$  plateau at the resonance  $T_i = 17\text{ms}$ , for  $g = 0.1007\text{mS/cm}^2 < g_c$  (left), and  $g = 0.1009\text{mS/cm}^2 > g_c$  (right). The broken line is the synaptic current with units shown on the right axis.

## 4.5. Poisson input

The distribution of initiation times of synaptic current pulses is now modeled as a Poisson process. The Gaussian noise term is absent,  $D = 0$ . Fig. 4.15 shows the average output frequency  $\bar{f}_o$  as a function of the input frequency  $f_i$  for two values of  $g_{syn}$ .  $\bar{f}_o$  evolves from  $\bar{f}_o \approx f_i$  at low frequencies to  $\bar{f}_o \approx 2f_i$  at high  $f_i$ .

Fig. 4.15 (right) presents the coefficient of variation as a function of  $T_i$  for the same values of  $g_{syn}$  as in Fig. 4.15 (left). The CV is only weakly dependent on  $g_{syn}$ . It approaches 1 in the high-frequency regime. The crossover between the small variation of output ISI and the high-variability regime occurs around  $T_i \approx T_{0res}$ , where  $CV \approx 0.5$ . This time scale is another way to understand the meaning of the neuron's resonance: it separates the low-variability regime from the high-variability regime for Poissonian inputs.

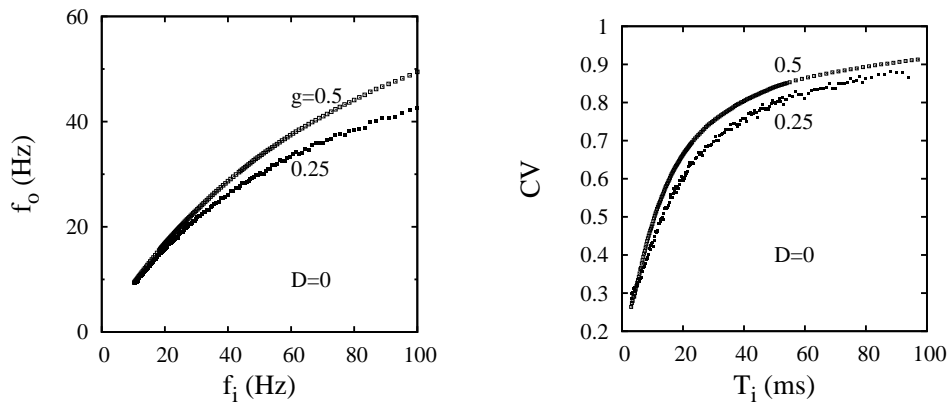


Figure 4.15: Left: The average output frequency as a function of the average input frequency for  $g_{syn} = 0.25\text{mS/cm}^2$  and  $g_{syn} = 0.5\text{mS/cm}^2$ . Right: The coefficient of variation as a function of  $T_i$  for the same values of  $g_{syn}$ .

## 5. Pulse packets

### 5.1. Response to an isolated spike

In this section we consider the dependence of the excitation threshold on the properties of a single current pulse. Does the threshold stimulus amplitude needed for the neuron to spike depend on the detailed form of the time dependence of the stimulus? How does the critical synaptic conductance  $g_c$  depend on the width of the pulse? These are some of the naturally arising questions in the studies of excitable cells [Blair, 1932a,b, Sahin and Tie, 2007].

Attempts to derive an analytical and approximate approach to the problem of a single spike in the HH model met with limited success [Kirstler et al., 2001, y Arcas et al., 2003]. Basic insight into the spike generation mechanism and the interaction of neighboring spikes can be obtained e.g. by studying the phase-resetting curve (PRC) and the spike-triggered average [Ermentrout et al., 2007]. The latter approach is based on the fact that for small stimuli  $x(t)$  any stable limit cycle oscillator can be reduced to a scalar model of its phase,

$$\frac{d\theta}{dt} = 1 + \Delta(\theta)x(t). \quad (5.1)$$

Here  $\theta$  varies between 0 and  $T$ ,  $T$  being the natural period.  $\Delta(\theta)$  is the PRC, which determines whether the incoming spike would accelerate the appearance of the next spike or delay it.

The study of response of the HH neuron to stimuli of different shapes improves our understanding of the dynamics of the model. It may also bring advances in applications such as deep brain stimulation [McIntyre et al., 2004]. Recent efforts in this direction [Wessale et al., 1992, Sahin and Tie, 2007, Hofmann et al., 2009] indicate the need for the fine-tuning of the stimulus waveform, depending on the needs of each neural stimulation application and available technology.

It should be kept in mind that the firing threshold  $g_c$  is not an extremely well defined quantity [Guckenheimer and Oliva, 2002, Clay, 2005]. The evidence in the literature as well as results in Chapters 2 and 3 of this work prove that  $g_c$  is not a smooth hyperplane in the parameter space. It is rather a complicated set of points that only roughly resembles a hyperplane. The values of  $g_c$  calculated in this chapter, however, can be viewed as well defined quantities since we

are looking at scales much larger than the irregularities in the set of points defining  $g_c$ .

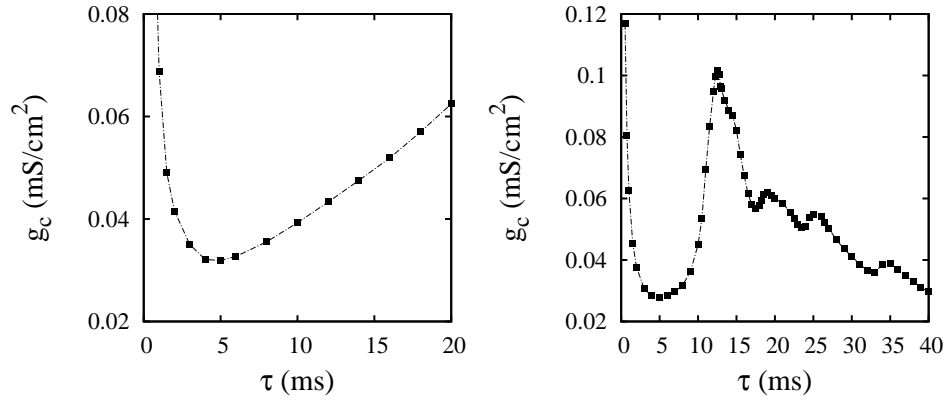


Figure 5.1: Dependence of the excitation threshold on the half-width of a single conductance pulse for  $T_i = 200$ ms (left),  $T_i = 18$ ms (right), when the pulse has the form of an inverted parabola,  $(1 - (t/\tau - 1)^2)\Theta(t)\Theta(2\tau - t)$ .

Fig. 5.1 presents the threshold as a function of the pulse half-width. A series of local minima in Fig. 5.1 (right) is a result of an interference between consecutive pulses. The optimal width of the rising side of the signal is approximately  $\tau \simeq 5$ ms. It is not beneficial to have larger  $\tau$ . Large  $\tau$  would result in higher peak current but it would interfere with response to the next pulse. We can now reinterpret the main resonance time scale discussed in Chapter 2 as being really the sum of the optimum duration of the signal increase, which in our calculation turned out to be about 5 – 6ms, and the refractory time, approximately 10 – 12ms.

## 5.2. Response to a cluster of spikes

Let us now replace a single pulse by a cluster of several spikes. The entire signal is now a periodic train of identical packets of spikes. Spikes in each packet are distributed periodically. Clusters are widely separated from each other so that we can neglect the dynamic interference between them. In the calculations we assume  $T_i = 200$ ms, where  $T_i$  is the interval between arrival times of spike packets.

We investigate the dependence of the critical synaptic conductance on the width of the cluster and on the half-width  $\tau$  of individual spikes. Within each cluster the spikes are spaced regularly, e.g. in a cluster of four spikes with  $T_0 = 30$ ms a new pulse starts every 7.5ms.

Fig. 5.2 (left) displays results for the case when the single pulse is a positive half of the sine waveform. The three curves correspond to different number of

pulses within the cluster. The optimal width of the packet is of the order of the main neuron resonance, 15 – 20ms. Fig. 5.2 (right) shows the threshold for a cluster of  $\alpha$  pulses separated by  $\tau$ , when the width of the cluster is varied.

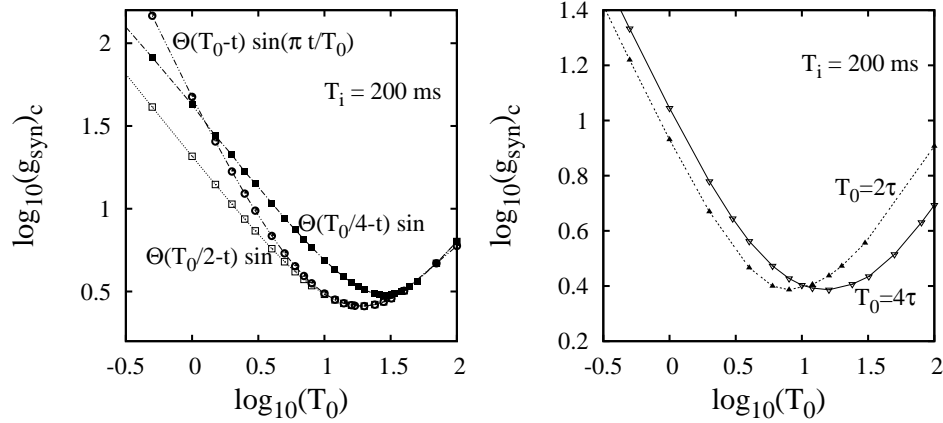


Figure 5.2: Left: The excitation threshold as a function of the width of a cluster of one (circles), two (open squares) and four (filled squares) equally spaced pulses when the single pulse is a positive part of the sine wave (left). Right: The excitation threshold as a function of the width of a cluster of two and four pulses separated by  $\tau$ , when the single pulse is an  $\alpha$  function,  $(t/\tau)exp(-t/\tau)$ .

In Fig. 5.3 we look at the dependence of  $g_c$  on the functional form of the time dependence near the peak of the conductance pulse,

$$g(t) = g_{syn}[\Theta(T_0/2 - t)(2t/T_0)^a + \Theta(t - T_0/2)(2 - 2t/T_0)^a]\Theta(T_0 - t). \quad (5.2)$$

Although these shapes of  $g(t)$  are not physiologically relevant, except for artificial stimulation such as DBS, it is useful to understand the dependence of  $g_c$  on  $a$  in more detail. The  $a = 0$  case is the usual rectangular waveform.

It is more appropriate to plot the scaled versions of Figs. 5.2 and 5.3, where  $g_c$  is scaled by the time integral  $\int g(t)dt$  over the entire cluster, which for fixed potential difference is proportional to the threshold charge. Fig. 5.4 shows all curves from Figs. 5.2 and 5.3 after scaling. The minimum  $g_c$  occurs between 4ms and 10ms.

It is clear that in the limit of narrow clusters all functional forms of single pulses give similar behavior. It is not exactly the particular functional form that matters but the rate of increase of the signal weight.

There is another interesting aspect of this phenomenon. If the preferred incoming pulse cluster width is of order 6 – 8ms, what happens if the time interval between subsequent pulses is of similar magnitude? This question was answered in Chapter 2: in this case we should have an anti-resonance, where the excitation threshold reaches its maximum for given  $T_i$  and  $\tau$ .

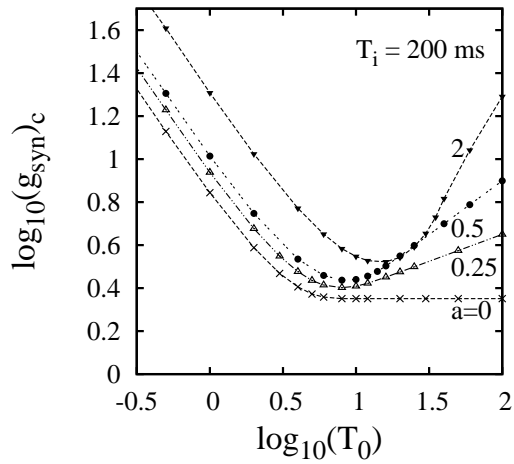


Figure 5.3: The excitation threshold as a function of the width of a cluster of eight equally spaced pulses. The curves are labeled by the exponent of the time dependence of a single pulse near the peak conductance,  $(\Theta(T_0/2 - t)(2t/T_0)^a + \Theta(t - T_0/2)(2 - 2t/T_0)^a)$ .

The optimum (resonant) pulse width is a time scale implied by the existence of the neuron's own resonant frequency and refractoriness. These are common properties of many different types of cells. Therefore we can expect that similar resonances related to the details of pulse (or cluster) shapes and time scales exist in different nervous systems.

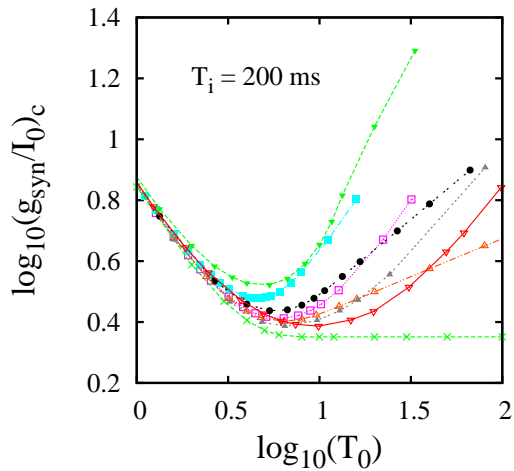


Figure 5.4: The thresholds  $g_c$  from Figs. 5.2 and 5.3 after scaling by the time integral  $I_0 = \int g(t)dt$  over an entire cluster.

## 6. The Hodgkin-Huxley network

*In vivo* recordings of neuronal discharge in mammalian cortex are usually highly variable. This variability is preserved at each stage of the processing path [Shadlen and Newsome, 1998]. It may come from a Poisson distribution of action potentials in the presynaptic neurons which translates into random excitatory and inhibitory postsynaptic conductances. Other sources of irregularity are typically assumed to be associated with the intrinsic cell dynamics and to be the Gaussian white noise or colored noise.

Tiesinga et al. [Tiesinga et al., 2000] investigated the dependence of the firing rate and the CV of the HH neuron on the properties of the stochastically fluctuating input current in the context of *in vivo* experiments. They also tried to model the main characteristics of *in vitro* measurements. The random stimulus consisted of a white-noise current and Poissonian postsynaptic conductances. It was found [Tiesinga et al., 2000] that the two sources of randomness affect the neuron response differently.

We would like to point out that another source of variability should also be taken into account: the intrinsic deterministic nonlinear dynamics of the neuron cannot be neglected. It has a significant effect near the excitation threshold and at high frequencies.

In this Chapter we analyze the response of a Hodgkin-Huxley neuron to inputs originating from 100 – 1200 identical HH neurons. Stochastic terms are absent and we focus mainly on understanding the consequences of the nonlinear dynamics of a single neuron in the network setting. Synapses are divided into the excitatory and the inhibitory sets.

In the single-neuron dynamics the largest chaotic-like area in the  $T_i - g_{syn}$  plane is located between the  $k = 2$  and the  $k = 3$  states. The irregular and singular behavior are caused by the competition between the even and the odd ISI modes. First we consider the irregular high-frequency regime described in Chapter 2. A single neuron reacting to a regular spike train may be considered as a generator of a highly variable signal. Near the multimodal transition occurring between 5.5ms and 7ms the CV is of order 1. Is this variability preserved when such signal is delivered by many independent neurons to another neuron? What is the relation between the firing rate and the CV? Can we find any universal features of the response of such a network fragment? These are some of the questions we would like to answer.

We assume that all HH neurons are identical and described by the following equation for the membrane potential,

$$C \frac{dV}{dt} = -I_{Na} - I_K - I_L - I_{syn} + I_{ext} + I_{noise}, \quad (6.1)$$

where  $I_{ext}$  is the applied current. Here we drop the stochastic term not related to the synaptic dynamics,  $I_{noise} = 0$ . The synaptic current is given by

$$I_{syn} = g_e s_e(t)(V - E_e) + g_i s_i(t)(V - E_i), \quad (6.2)$$

where  $g_e = g_i = 2\text{mS/cm}^2$  are the maximum excitatory and inhibitory conductances respectively,  $E_e = 0\text{mV}$  and  $E_i = -75\text{mV}$  are the excitatory and inhibitory reversal potentials. All other parameters are the same as in Chapter 2.

The ratio of inhibitory to excitatory synapses,  $r = N_i/N_E$ , is allowed to vary between 0 and 1. The total number of neurons is  $N = N_i + N_E$ . If it is not explicitly said otherwise, calculations are performed with the assumption  $r = 0.2$  which is typical for a mammalian neocortex. The arrival of postsynaptic potentials from different synapses is uncorrelated. Individual synaptic events are modeled as instantaneous increase of the conductance,  $\Delta s_e = 0.001$  and  $\Delta s_i = 0.005$ , followed by exponential decay with  $\tau_e = 2\text{ms}$  for the excitatory synapse and  $\tau_i = 10\text{ms}$  for the inhibitory synapse. The crossing of  $V = 0\text{mV}$  from below is identified as an emission of spike.

Our calculation is done here in two stages. First a periodic conductance input of the form used in Chapter 2 is delivered to each neuron in the pool, using different statistically independent initial conditions for each neuron and assuming identical values of the synaptic conductance  $g_{syn}$  in each neuron. The dynamics of each of the input neurons evolves independently. Next the resulting spike trains are used to trigger synaptic transmission to the output neuron, following Eqs. 6.1 and 6.2.

We start by generating nonlinear inputs at  $T_i = 7\text{ms}$ . The CV as a function of the average output frequency of the neuron is shown in Fig. 6.1.

The CV is at most very weakly dependent on  $r$ , see Fig. 6.2. The calculation was done for the average output frequency  $f_o = 35\text{Hz}$ , for  $N_E = 500$  and  $1000$ . The input neurons were all stimulated by a periodic spike train of  $\alpha$  functions arriving every  $T_i = 7\text{ms}$ .

Fig. 6.3 shows the linear dependence of frequency on the synaptic conductance near the threshold. Results for different values of  $N_E$  are almost identical after rescaling  $g_{syn}$  by  $1000/N_E$ . For slightly larger  $T_i$  the linearity holds all the way down to  $f_o = 0$ .

The anti-resonance near  $T_i = 7\text{ms}$  shows up in the network setting as a triangular non-firing zone. The network preserves the singularity of the firing rate originating from the competition of the odd and the even ISI modes (see Chapter 2).

In the perithreshold regime the ISI histogram is dominated by the low-order and high-order modes. The intermediate modes, between  $T_o = 100\text{ms}$  and

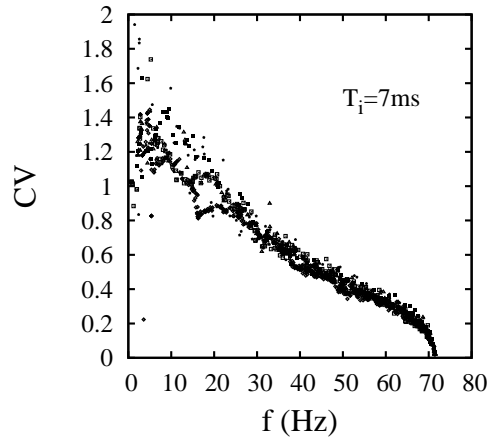


Figure 6.1: The coefficient of variation vs. average firing frequency in the output neuron for  $N_E = 100, 200, 300, 400, 500, 1000$ .

1000ms are absent within  $10^{-3}\text{mS/cm}^2$  of  $g_c$ . The multimodal transition survives in the network in a somewhat altered form. In Fig. 6.5 (right) the odd modes dominate the left side of the diagram. This clearly tells us that the multimodal odd-all transition is not related to any particular form of the stimulus. It is a manifestation of the intrinsic dynamics of the neuron.

Fig. 6.6 shows the multimodal plot of the ISI as a function of the conductance close to the excitation threshold at  $T = 13.85\text{ms}$ . The right edges of the

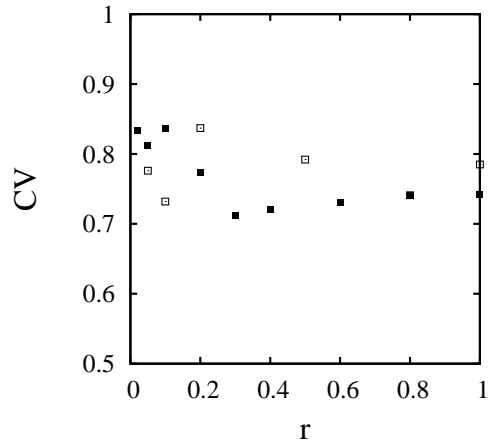


Figure 6.2: The coefficient of variation of the ISI is at most very weakly dependent on  $r$  if the frequency  $f_o$  is fixed. The graph shows results at  $f_o = 35\text{Hz}$  and  $N_E = 500$  (empty squares) and  $N_E = 1000$  (full squares).

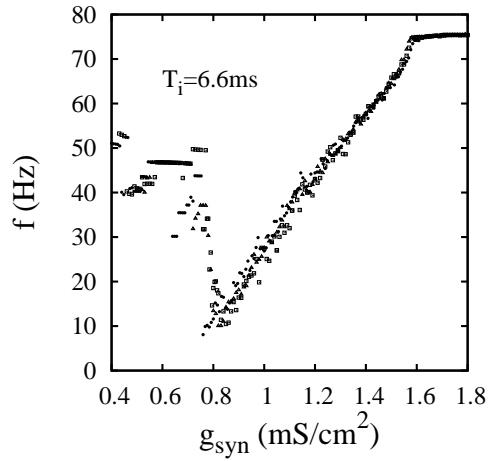


Figure 6.3: The average frequency vs. the synaptic conductance for  $T_i = 6.6\text{ms}$ . The simulation was performed for  $N_E = 100, 200, 500, 1000$ . In each data set the  $g_{syn}$  coordinate was rescaled in the following way:  $g_{syn} \rightarrow g_{syn}1000/N_E$ . The relationship between  $f_o$  and  $g_{syn}$  is almost perfectly linear between  $g_{syn} = 0.8\text{mS/cm}^2$  and  $1.6\text{mS/cm}^2$ . The linearity does not extend down to  $f_o = 0$  due to the proximity to the  $k = 3$  state.

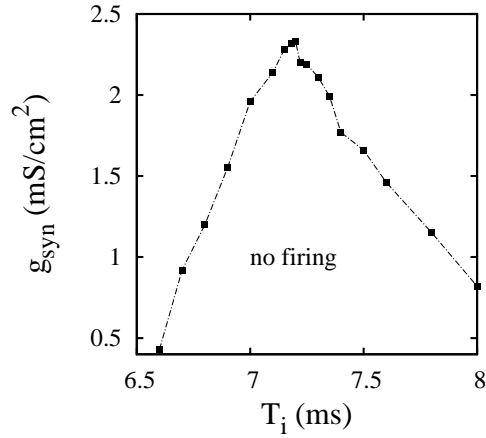


Figure 6.4: The dependence of the excitation edge on  $T_i$ . There is a pronounced anti-resonance effect. Input neurons were stimulated by periodic spike trains with randomly selected initial conditions and  $T_i = 7\text{ms}$ .

ISI clusters seem to scale  $\sim (g_{syn} - g_c)^{3/2}$ , where  $g_c$  is the excitation threshold. However a more detailed study is needed to verify this relation.

The ISI distribution in both Figs. 6.5 and 6.6 has two dominant parts near  $g_c$ : the gamma frequency component (40-80 Hz) and a low frequency component of  $f \sim 1\text{Hz}$ . Somewhat similar bimodal frequency histogram was obtained in

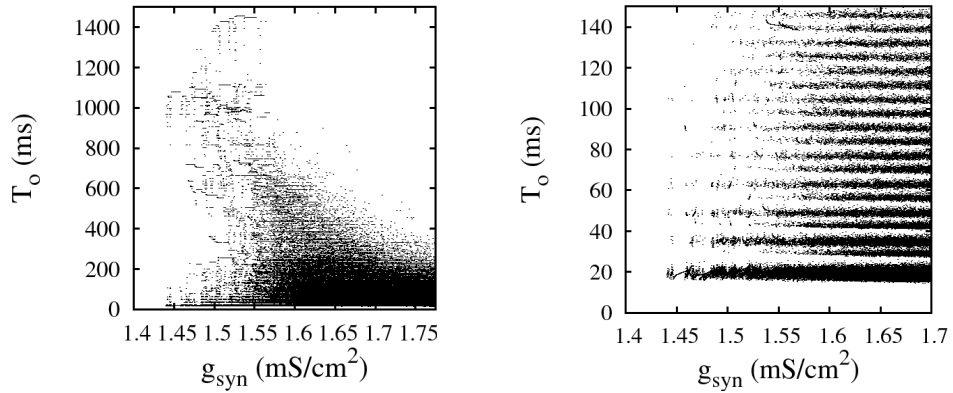


Figure 6.5: Left: ISI as a function of the synaptic strength in the Hodgkin-Huxley neuron receiving input from a pool of 1000 excitatory and 200 inhibitory synapses. Right: Low-order ISI clusters. The odd modes clearly dominate. Here  $T_i = 6.9$ ms.

the stochastic computation with a channel noise in a single HH neuron [Rowat, 2007]. This type of ISI distribution arises when bursts of spikes are separated by long periods of silence. It is quite significant that both the stochastic single neuron model [Rowat, 2007] and the deterministic network model give the same general form of ISIH. This seems to be a general feature of the HH model. Our explanation is the multistability of the solution to HH equations in the

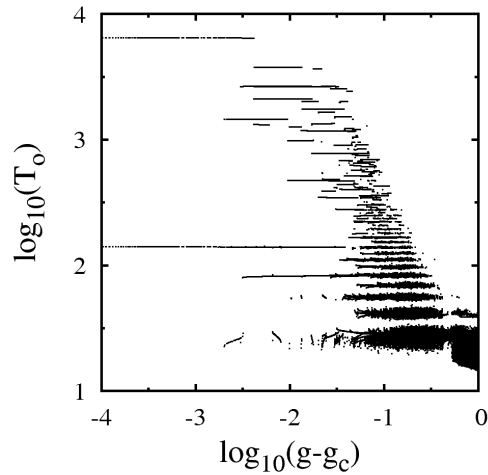


Figure 6.6: Logarithmic plot of the ISI as a function of the synaptic strength in the Hodgkin-Huxley neuron receiving input from a pool of 1000 excitatory and 200 inhibitory synapses. Here  $T_i = 13.85$ ms. The scaling exponent of the right edges of the ISI is close to  $3/2$ .

perithreshold regime, analogous to the bistability between e.g. the  $k = 2$  state and the nonfiring state which appears nearby in the response diagram (see Fig. 3.1). The multimodality evolving towards the bimodality can also be seen in Fig. 6.6. The dominant mode is  $k = 2$ . The higher modes gradually disappear as the threshold is approached from above. Similar effect occurs elsewhere within the resonant regime near  $T_i = 17.5\text{ms}$ , where the lowest order mode may coexist with some high-order modes. This effect is a deterministic one and does not require stochastic dynamics as suggested in Ref. [Rowat, 2007]. Bimodal distributions were recorded in mammalian neurons of different types (see e.g. [Nakahama et al., 1968, Siebler et al., 1993, Duchamp-Viret et al., 2005]).

The relation between the CV and the output frequency shown in Figs. 6.1 and 6.7 is universal and does not depend directly on the frequency of the input signal. For example the CV vs.  $f$  obtained for  $T_i = 29\text{ms}$  is nearly identical to that in Fig. 6.7 for  $T_i = 13.85\text{ms}$ . The dominant feature is the linear dependence on  $f_i$  below the lowest integer mode-locked plateau.

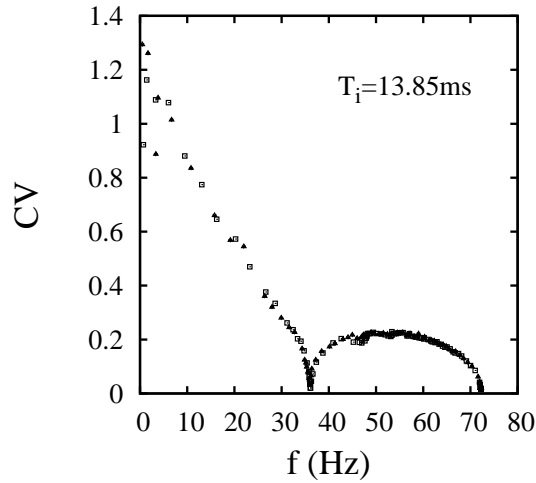


Figure 6.7: The coefficient of variation vs. average frequency of the output signal in the irregular regime at  $T_i = 13.85\text{ms}$ . The relation is independent of the number of input neurons. The squares and triangles correspond to  $N_E = 1000$ ,  $N_I = 200$  and  $N_E = 200$ ,  $N_I = 40$ , respectively.

Near the edge of the  $k = \text{const}$  plateau the CV scales with the exponent  $1/2$ . Fig. 6.8 shows the logarithmic plot of the CV vs.  $f_0 - f$ , where  $f_0$  is the frequency of the plateau.

A large number of synaptic inputs reduce time necessary to perform a reliable integration of stimuli. However the ISI coefficient of variation does not depend noticeably on  $N_E$  for fixed frequency, provided  $g_{syn}$  is scaled by  $N_E$ . Cortical neurons may receive inputs from about 3000-10000 synapses although not all of them need to be active. This is larger than the number of inputs considered here but the obtained results scale quite accurately with the number of inputs

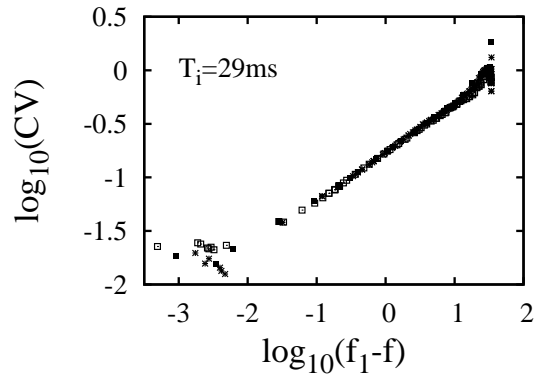


Figure 6.8: The scaling of the coefficient of variation vs. the average frequency of the output signal in the irregular regime at  $T_i = 29\text{ms}$ .  $f_1$  is the frequency of the  $k = 1$  plateau. The data points were obtained with  $N_E = 200, 500$ , and  $1000$ , keeping  $r = N_i/N_E = 0.2$ .

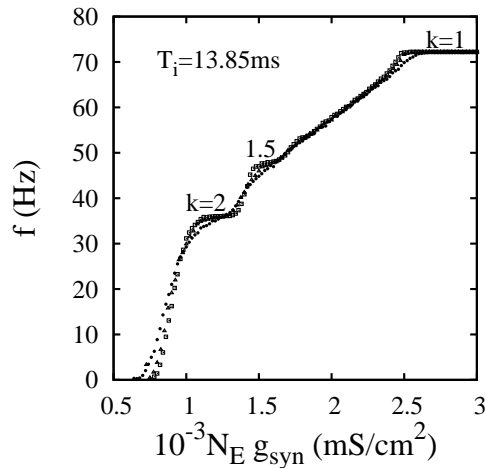


Figure 6.9: The output signal frequency vs. the synaptic strength in the regular regime at  $T_i = 13.85\text{ms}$ .

and results for a different number of identical input neurons can be predicted with a high precision.

Qualitatively similar dependence of the CV on the firing rate was obtained by [Prescott et al., 2008] in the simulations of the Morris-Lecar model with adaptation. The decrease of the CV with increasing  $f_o$  is also consistent with the calculations for the white noise driven and conductance driven HH neuron [Tiesinga et al., 2000].

The high variability due to the nonlinear dynamics of individual neurons at low output frequencies may explain the long-standing dilemma posed by Softky and Koch [Softky and Koch, 1993].

Assuming independent activity by each cortical neuron delivering input to the other cortical neurons one obtains a set of statistically independent excitatory postsynaptic potentials (EPSPs) with a constant mean rate. However this type of input gives a much smaller firing variability than that observed *in vivo*.

We showed that a perfectly periodic high-frequency signal delivered independently to each neuron in the network leads to a very high firing variability in the second and further layers of neurons. Also in the model studied here the input and output neurons have similar dynamic properties. The high variance is preserved.

Other types of inputs were not considered in this chapter. It remains to be seen whether this results also holds for less regular stimuli and for correlated inputs [Stevens and Zador, 1998].

We know from the information theory that the optimal code appears random. The nonlinearities in the HH-type model lead to firing characterized by high variability and thus, increased efficiency of coding. The real cortical neurons differ from the simplified HH model. Nevertheless similar nonlinearities may appear *in vivo*. They may be related to the presence of anti-resonances. It would be useful to try to find these anti-resonances and investigate their properties.

# 7. Regular spiking cortical cells

## 7.1. Introduction

The neocortex which is the basis of the cognitive functions of mammals forms about 80% of the human brain. The most common type of neurons in the neocortex are excitatory pyramidal neurons, accounting for about 75-80% of all neurons. The *in vivo* activity of cells in the cortex is highly variable (see e.g. [Mainen and Sejnowski, 1995, Buracas et al., 1998, Stevens and Zador, 1998, Harsch and Robinson, 2000], and many other works). One of the basic tasks in testing various models is to account for this high variability.

In this chapter we will use a minimum model which includes adaptation of the spiking frequency after the onset of the stimulus and is an essential feature of cortical neurons. The two main potassium currents usually considered in this context [Koch, 1999] are the AHP (calcium-dependent afterhyperpolarizing) and the M (slow, voltage-dependent, noninactivating muscarinic-sensitive) current. Blocking both of these currents eliminates almost all the adaptation [Yamada et al., 1989] and lowers the excitation threshold.

The simplest Hodgkin-Huxley equations modified for application to cells of the central nervous system [Traub and Miles, 1991] contain the usual potassium and sodium channels, the slow potassium current, and the calcium currents,

$$C \frac{dV}{dt} = -I_L - I_{Na} - I_K - I_M - I_{LT} - I_{HT} - I_{syn} + I_{app}. \quad (7.1)$$

Here  $I_M$  is a slowly-varying potassium current giving the spike-frequency adaptation.  $I_{HT}$  and  $I_{LT}$  are low-threshold and high-threshold calcium currents respectively which do not seem to play significant role in regular spiking cells and are omitted here. If the first-order kinetic scheme for the ionic channels is assumed, the currents have the form

$$I_j = g_j m^p h^r (V - E_j). \quad (7.2)$$

where  $g_j$  is the maximum conductance of the channel,  $m$  and  $h$  are activation and inactivation variables respectively and  $E_j$  is the reversal potential. The Na and K currents have the usual form,

$$I_{Na} = g_{Na} m^3 h (V - E_{Na}), \quad (7.3)$$

$$I_K = g_K n^4 (V - E_K), \quad (7.4)$$

where the  $m, h, n$  rates are given as usual,

$$\frac{dm}{dt} = \alpha_m(V)(1 - m) - \beta_m(V)m, \quad (7.5)$$

$$\frac{dh}{dt} = \alpha_h(V)(1 - h) - \beta_h(V)h, \quad (7.6)$$

$$\frac{dn}{dt} = \alpha_n(V)(1 - n) - \beta_n(V)n, \quad (7.7)$$

and have the following voltage dependence,

$$\alpha_m = \frac{-0.32(V - V_T - 13)}{\exp(-(V - V_T - 13/4)) - 1}, \quad (7.8)$$

$$\beta_m = \frac{0.28(V - V_T - 40)}{\exp((V - V_T - 40)/5) - 1}, \quad (7.9)$$

$$\alpha_h = 0.128 \exp(-(V - V_T - 17)/18), \quad (7.10)$$

$$\beta_h = \frac{4}{\exp(-(V - V_T - 40)/5) + 1}, \quad (7.11)$$

$$\alpha_n = \frac{0.032(V - V_T - 15)}{1 - \exp(-(V - V_T - 15)/5)}, \quad (7.12)$$

$$\beta_n = 0.5 \exp(-(V - V_T - 10)/40). \quad (7.13)$$

We will investigate the consequences of the slow voltage-dependent potassium current,

$$I_M = g_M w (V - E_K). \quad (7.14)$$

The variable  $w$  obeys the equation

$$\frac{dw}{dt} = \frac{w_\infty(V) - w}{\tau_w(V)}, \quad (7.15)$$

where

$$w_\infty(V) = \frac{1}{1 + \exp(-(V + 35)/10)}, \quad (7.16)$$

and

$$\tau_w(V) = \frac{\tau_{max}}{3.3 \exp((V + 35)/20) + \exp(-(V + 35)/20)}. \quad (7.17)$$

Here  $V$  is the membrane potential,  $C = 1\mu F/cm^2$  is the capacitance of the membrane,  $g_L$  is the resting conductance and  $E_L$  is the reversal potential of the leaking conductance. The time constant  $\tau_{max}$  is within the range 400ms to 4s.

In a recent study Pospischil et al. [Pospischil et al., 2008] fitted the HH-type models to the data from the most frequently occurring classes of cortical and thalamic neurons. Their approach is a minimalist one, aimed at obtaining simple ‘generic’, one-compartment models reproducing the salient features for each class of cells. This implies the use of the smallest possible set of the voltage-dependent conductances. It should be kept in mind, however, that there is no unique fitting procedure and different approaches using the same data set can lead to different sets of parameters. Both detailed and multi-compartment models including dendritic morphology and point neuron models are used in the fits. Even different parameter sets may lead to very similar behavior [Bhalla and Bower, 1993, Marder et al., 2007]. The most important step in fitting experimental data is the choice of the error function. The mean square deviation is of little use due to locally fast changes of  $V$ . A more reasonable approach aims at reproducing the qualitative features of  $V(t)$  [Druckmann et al., 2007, Pospischil et al., 2008] (although again the criteria for selecting important features in fitting to more complicated traces of  $V(t)$  are not unique).

Here we focus on the regular spiking class of neurons stimulated with the same periodic stimulus as in the earlier chapters. The differential equations are integrated, as before, using the fourth order Runge-Kutta algorithm with the time step of 0.01ms.

## 7.2. Regular spiking excitatory neuron

In this section we use two sets of model parameters from the literature and compare qualitative features of the response. The first set comes from Kopell et al. [Kopell et al., 2000]. In this case the conductances are  $g_L = 0.1mS/cm^2$ ,  $E_L = -67mV$ ,  $g_{Na} = 100mS/cm^2$ ,  $E_{Na} = 50mV$ ,  $g_K = 80mS/cm^2$ ,  $E_K = -100mV$ , and  $\tau_{max} = 400ms$ . The current  $I_{syn}$  is modeled in the same way as in Chapters 2 and 3.  $T_i$  is the interspike separation of a perfectly periodic input. The response diagram is shown in Fig. 7.1.

Voltage peaks with  $V_{max} > 0mV$  are treated as spikes. With no inhibition there is a weak resonance at  $T_i \simeq 10ms$ . The increase of  $g_M$  raises the threshold to larger values of  $g_{syn}$ . It also leads to a development of an anti-resonance at  $T_i$  between 10ms and 20ms.

The second set of data comes from the studies of the rat somatosensory cortex *in vitro* [Pospischil et al., 2008]. The following parameters were used:

$g_L = 0.0205mS/cm^2$ ,  $E_L = -70.3mV$ ,  $g_{Na} = 56mS/cm^2$ ,  $E_{Na} = 50mV$ ,  $V_T = -56.2mV$ ,  $g_K = 6mS/cm^2$ ,  $E_K = -90mV$ ,  $g_M = 0.075mS/cm^2$ ,  $\tau_{max} = 608ms$ .

Fig. 7.2 shows the response diagram of regularly spiking neurons, in the  $g_{syn} - T_i$  plane. The boundaries of the mode-locked regions were drawn by discarding the initial 1s of data.

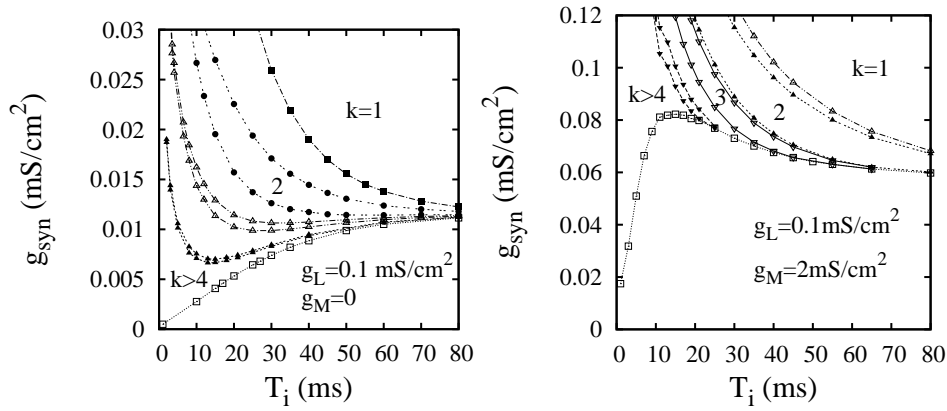


Figure 7.1: The asymptotic response diagram for  $t \gg \tau_{max}$ , after the initial adaptation has run its course, for  $g_M = 0$  (left),  $g_M = 2\text{mS}/\text{cm}^2$  (right). The leak conductance is  $g_L = 0.1\text{mS}/\text{cm}^2$  in both cases.

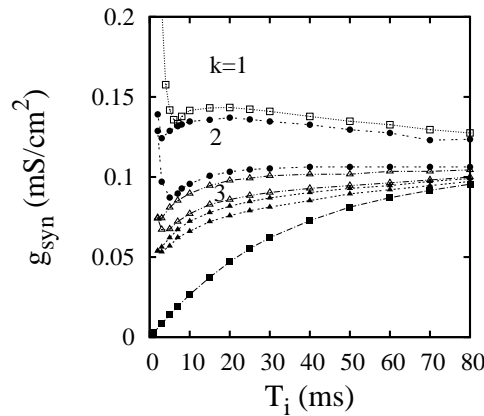


Figure 7.2: The asymptotic response diagram of the regular spiking excitatory neuron based on data from [Pospischil et al., 2008]. There is a resonance below  $T_i = 10\text{ms}$ .

Figs. 7.1 and 7.2 differ at high frequencies. The parameter set of Ref. [Pospischil et al., 2008] gives preferential response at  $f_i \approx 100 - 120\text{Hz}$ . No similar resonance appears in the data set of Ref. [Kopell et al., 2000] (see Fig. 7.1). It would be interesting to verify the existence of this resonance experimentally.

Fig. 7.3 offers another view of this effect. The tendency to spike at certain frequency manifests itself also as an increased length of the initial interval where the response is locked 1:1 to the stimulus. The transition between the short-term dynamics and the asymptotic one occurs suddenly. In Fig. 7.3 (left) the switch from  $k = 1$  to  $k = 2$  response occurs without adaptation, within a fraction of  $T_i$ . There is also a very interesting effect related to the parity of the modes.

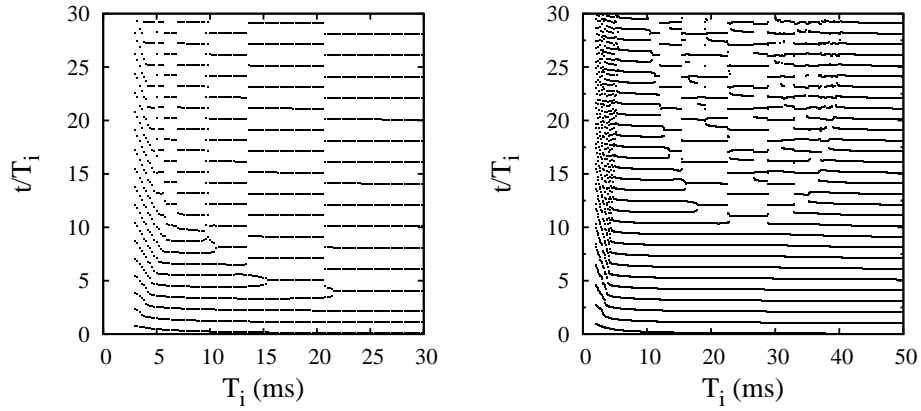


Figure 7.3: The firing times scaled by the stimulus period in response to a periodic set of conductance pulses of the  $\alpha$ -type,  $g_{syn} \sim t \exp(-t/\tau)$ . The synaptic conductance is (a)  $g_{syn} = 0.125 \text{mS/cm}^2$  (left),  $g_{syn} = 0.138 \text{mS/cm}^2$  (right).

In Fig. 7.3 (left) at  $T_i = 25 - 30 \text{ms}$  the switch from  $f_o = f_i$  to  $f_o = f_i/2$  occurs after the emission of the second spike. The third spike is missed and the fourth spike appears. The oscillation continues then with the reduced frequency. It appears as if only the even spikes survived. Between  $T_i = 15 \text{ms}$  and  $20 \text{ms}$  the third spike still appears but now the fourth spike is missed and the oscillation continues with odd-only spikes. Below  $T_i = 15 \text{ms}$  the long-term spike parity changes again. The asymptotic firing rate relative to the stimulus frequency remains the same, with the cell being mode locked 2:1, but the parity of the spike train alternates as a function  $T_i$ .

This type of dynamics may influence the synchronization properties and switching between the gamma (30-80 Hz) and beta (12-30 Hz) cycles in the brain. This might lead to sub-synchronization of the network into two populations of neurons firing out of phase. We could then tune other pools of neurons connected to this network to either  $k = 1$  or  $k = 2$  dynamics by small adjustments of the coupling strength.

The ISI return maps in the high-frequency regime are shown in Fig. 7.4. There is a clear single mode dynamics and there is no mixing of different modes.

The nonlinearities found in this model neuron were of moderate size. The ISI coefficient of variation was always below 0.5. In contrast to the HH model with the 'standard' parameter set the largest values of the CV were obtained at the edge of the  $k = 1$  locked state. Near the threshold CV disappeared linearly as a function of  $g_{syn} - g_c$ , where  $g_c$  is the threshold synaptic conductance. This means that the solution manifold is quite different from the HH model studied in the preceding chapters of this work, where the CV reached its maximum in the perithreshold regime. However this should not be surprising since excitatory neurons in the cortex spike regularly with low variation and have relatively simple dynamic properties.

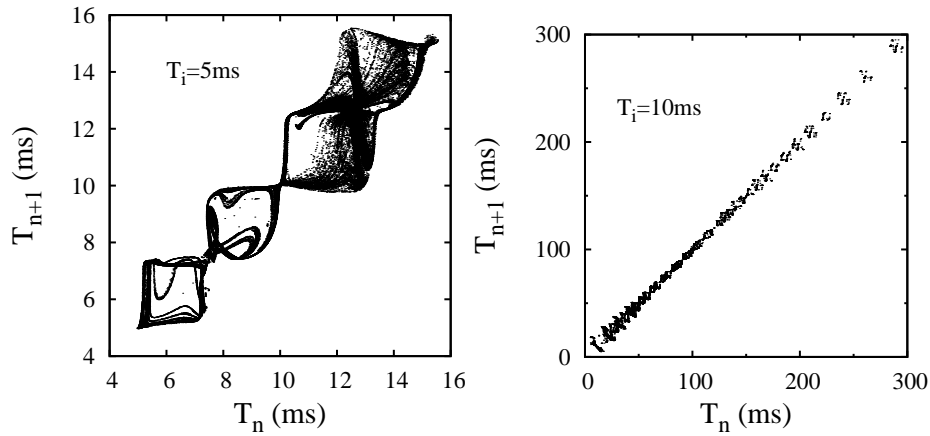


Figure 7.4: Return maps of the output ISI of a regular spiking excitatory neuron, for  $T_i = 5\text{ms}$  (left),  $T_i = 10\text{ms}$  (right), obtained by varying the synaptic conductance between 0 and  $2\text{mS}/\text{cm}^2$ .

### 7.3. Regular spiking inhibitory neuron

Here we use the parameter sets obtained by fitting the one-compartment HH type of model to experimental data from the rat somatosensory cortex *in vitro* [Pospischil et al., 2008]:

$g_L = 0.0133\text{mS}/\text{cm}^2$ ,  $E_L = -56.2\text{mV}$ ,  $g_{Na} = 10\text{mS}/\text{cm}^2$ ,  $V_T = -67.9\text{mV}$ ,  $g_{Kd} = 2.1\text{mS}/\text{cm}^2$ ,  $g_M = 0.098\text{mS}/\text{cm}^2$ ,  $\tau_{max} = 934\text{ms}$ . The other quantities are the same as for the excitatory neuron.

The response diagram is shown in Fig. 7.5. It differs substantially from results for the excitatory neuron in Fig. 7.2. Most importantly there is a lack of a clear excitation threshold at finite  $T_i$ . The neuron responds with low frequency oscillations even at very small  $g_{syn}$ . Below  $T_i = 20\text{ms}$  the boundary of the  $k = 1$  state is nonmonotonic. After reaching a local maximum, it goes through a minimum and finally rises very steeply at about  $T_i = 5\text{ms}$ .

The local minimum is associated with a resonance where the response is locked 1:1 to the input without inhibition. Figs. 7.6 and 7.7 show the firing times scaled by the mean ISI of the stimulus. The switch from the initial response to the long-time dynamics occurs on the scale of one  $T_i$ . The boundary between the two regimes is most pronounced near the  $k = 1$  state where the synaptic coupling is stronger. Between the mode-locked states with integer  $k$  the long-time dynamics may be highly irregular, despite initially regular response (e.g. at  $T_i = 30\text{ms}$  and  $T_i = 80\text{ms}$  in Fig. 7.6 (right)).

The deterministic interval return map in Fig. 7.8 shows some similarity to the measurements of Harsch and Robinson [Harsch and Robinson, 2000], where the stimulation consisted of Poisson AMPA (fast excitatory) unitary conductance transients and unitary Poisson AMPA + NMDA. It is therefore interesting to note

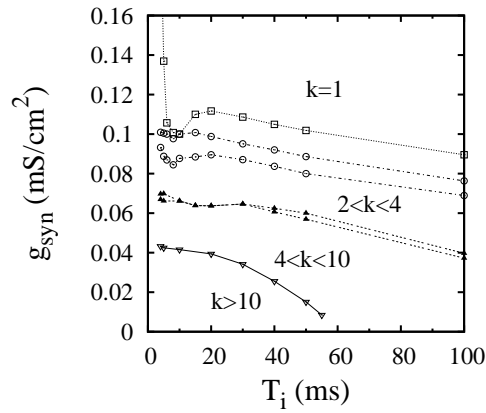


Figure 7.5: The asymptotic response diagram,  $t \gg \tau_{max}$ , of a regular spiking inhibitory neuron based on data from [Pospischil et al., 2008]. There is a resonance close to  $T_i \approx 10\text{ms}$  and anti-resonance at  $T_i \approx 20\text{ms}$ . Only the two lowest ISI modes occupy significant areas of this diagram (the  $k = 2$  mode is located between the empty circles).

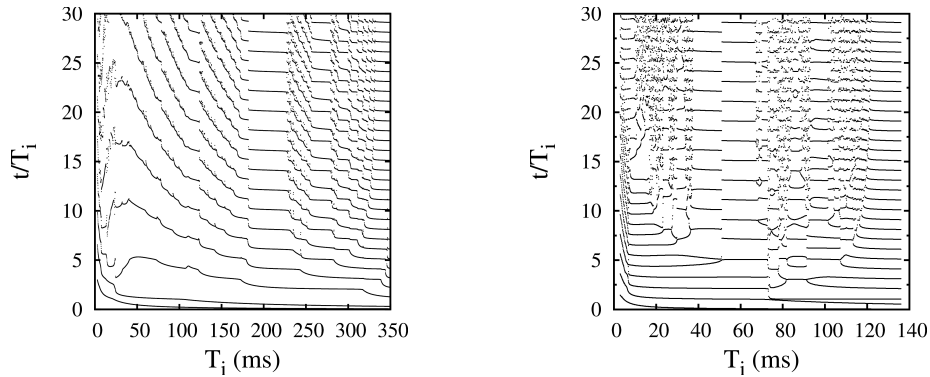


Figure 7.6: The firing times of an inhibitory neuron scaled by the input period in response to a periodic set of the  $\alpha$ -type conductance pulses. The synaptic conductance is  $g_{syn} = 0.025\text{mS/cm}^2$  (left)  $g_{syn} = 0.075\text{mS/cm}^2$  (right) Note the anti-resonance below  $T_i = 50\text{ms}$  (left).

that the general form of the return map is not very sensitive to the type of input, deterministic or stochastic one.

Typical relations between the CV and the output frequencies are shown in Fig. 7.9. Maximum CV values are weakly dependent on  $T_i$  and almost always are near  $0.4 - 0.5$ . We found only one exception: for  $T_i = 50\text{ms}$  the maximum CV was  $0.7$  but this occurred in a very narrow interval of  $g_{syn}$ . The irregularity of the CV comes from the existence of doublets and higher-order bursts for stronger inputs.

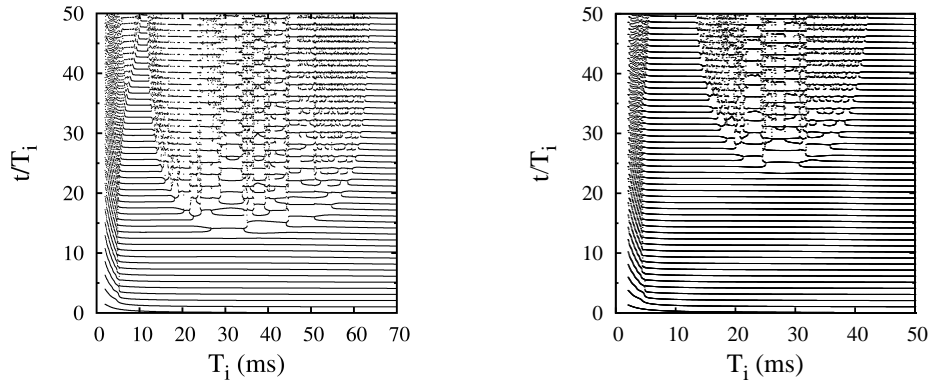


Figure 7.7: The firing times of an inhibitory neuron in response to a periodic set of the  $\alpha$ -type conductance pulses. The synaptic conductance density is  $g_{syn} = 0.1\text{mS}/\text{cm}^2$  (left),  $g_{syn} = 0.112\text{mS}/\text{cm}^2$  (right). In both diagrams the signal is strong enough to maintain the 1:1 locking initially. Eventually, however, the dynamics becomes irregular with  $k > 1$ .

It is difficult to explain high values of the *in vivo* CV solely by either a stochastic mechanism, e.g. random inhibition [Tateno and Robinson, 2006], or by a nonlinear mechanism (see Fig. 7.9). There is some evidence that in regular spiking neurons the response to correlated inputs is associated with higher CV [Koch, 1999]. Therefore one way to obtaining  $CV \sim 1$  may be based on correlated inputs with some stochastic mechanism and nonlinearity of neuron's response.

The firing times of the initial two peaks as a function of  $g_{syn}$  is shown in Fig. 7.10. The ISI between the two peaks can be continuously tuned by altering

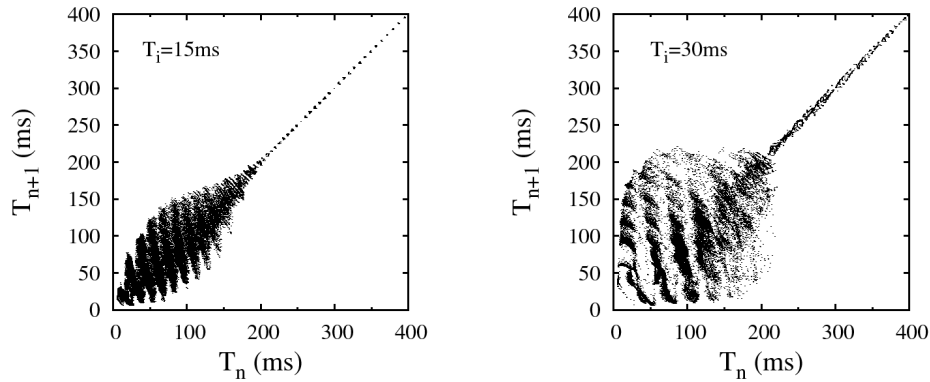


Figure 7.8: Return maps of the output ISI of a regular spiking inhibitory neuron, for  $T_i = 15\text{ms}$  (left),  $T_i = 30\text{ms}$  (right), obtained by varying the synaptic conductance. These results resemble experimental results obtained on rat cortical neurons [Harsch and Robinson, 2000], where the off-diagonal correlations have a time scale of 200ms.

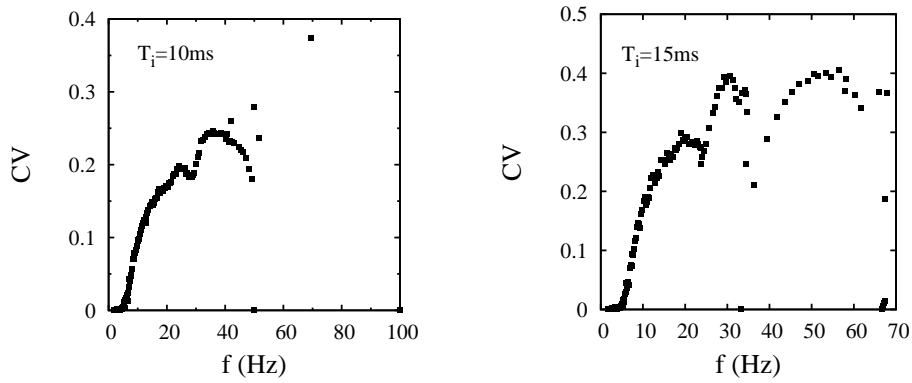


Figure 7.9: The coefficient of variation vs. the output frequency for  $T_i = 10\text{ms}$  (left),  $T_i = 15\text{ms}$  (right), obtained by varying the synaptic conductance  $g_{syn}$  between 0 and  $2\text{mS}/\text{cm}^2$ .

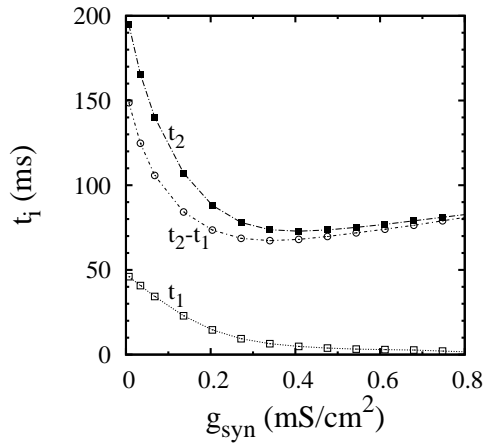


Figure 7.10: The first two preferred firing times vs. the synaptic conductance  $g_{syn}$  in the response of the regular spiking inhibitory neuron. The onset of the stimulus is at  $t = 0$ . The second peak has a minimum at an intermediate value of  $g_{syn}$ .

the synaptic conductance. There is a weak resonance at  $g_{syn} = 0.3\text{mS}/\text{cm}^2$ . Increasing  $g_{syn}$  beyond this value inhibits the second peak. This 'repulsion' of subsequent peaks is due to the emergence of secondary voltage peaks following the main one (see the next Section).

Near the resonance at  $T_i \approx 5\text{ms}$  there is significant rearrangement of the firing times (see Fig. 7.11). For intermediate values of  $g_{syn}$  there is a gap in the neuron's response. The spikes voltage maximum falls below  $V = 0\text{mV}$ . We will see in the next Section that this phenomenon is related to the appearance of bursts with the bursting period of approximately  $4\text{ms}$ .

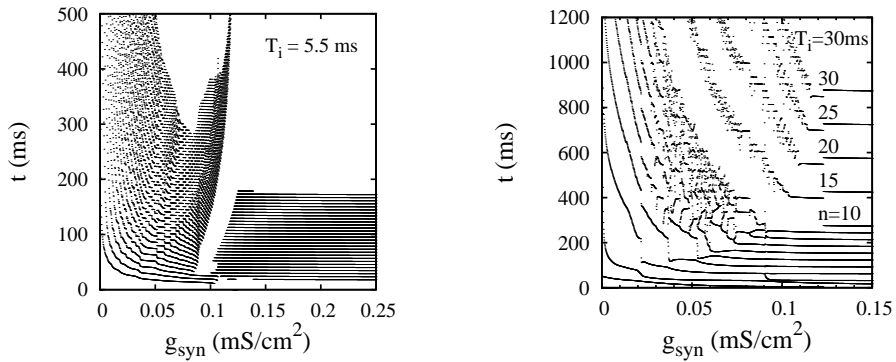


Figure 7.11: The response of the regular spiking inhibitory neuron as a function of  $g_{syn}$ . The initial 30 peaks at  $T_i = 5.5\text{ms}$  (left),  $T_i = 30\text{ms}$  (right). Near  $T_i = 5\text{ms}$  there is a sudden reorganization of the cell's response. For  $g_{syn} \approx 0.1\text{mS}/\text{cm}^2$  the neuron emits only a few spikes and the subsequent voltage peaks are below  $V = 0$ . For larger  $g_{syn}$  the response is perfectly periodic with no inhibition.

## 7.4. Poisson input

Here we assume that the timings of presynaptic spikes are Poisson-distributed. We would like to know if the feature shown in Fig. 7.10, when the stimulus was ideally periodic, appears also in the case of typical stochastic input.

Fig. 7.12 shows a raster of 1000 trials with different seeds, all other parameters unchanged, for  $g_{syn} = 0.1\text{mS}/\text{cm}^2$  and  $T_i = 30\text{ms}$ . There is a high probability the cell will fire at two precisely determined moments despite randomness of the input. There are somewhat similar experimental results on MT cells of behaving monkeys [Bair and Koch, 1996], where the cells reliably fired in response to the same random dot movie shown many times. Thus the reliability of firing at two precisely determined moments after the onset of stimulus is not directly related to the statistics of the input, although it depends on it to some extent. The reliability is higher for distributions with higher mean interspike separation. Reports in the literature point out consistently the high variability and the high precision of response to Poisson inputs [Mainen and Sejnowski, 1995, Harsch and Robinson, 2000].

The output ISI histogram is shown in Fig. 7.13. While the initial peak and the exponential tail resemble the Poisson distribution, in the range between 30ms and 300ms the histogram significantly deviates from it. We may conclude that the regular spiking inhibitory neuron transforms most significantly the intermediate part of the distribution. This is to be expected, if we look at Fig. 7.8, where we see significant correlations of subsequent intervals between 20ms and 250ms.

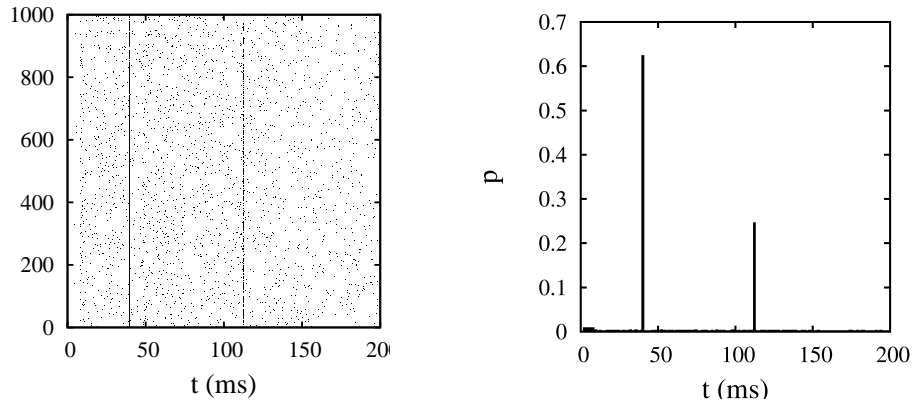


Figure 7.12: The initial response to a set of Poisson-distributed  $\alpha$  functions with  $g_{syn} = 0.1\text{mS}/\text{cm}^2$  and  $T_i = 30\text{ms}$  Left: Firing times for a set of 1000 trials with different seeds. The trial number is shown on the vertical axis. The onset of stimulus is at  $t = 0$ . Right: Relative frequency of occurrence of the initial firing times in the set of 1000 different initial conditions.

The emergence of an exponential tail at large  $T_i$  implies that events at these time scales are independent. In other words the system lost memory of the previous spike.

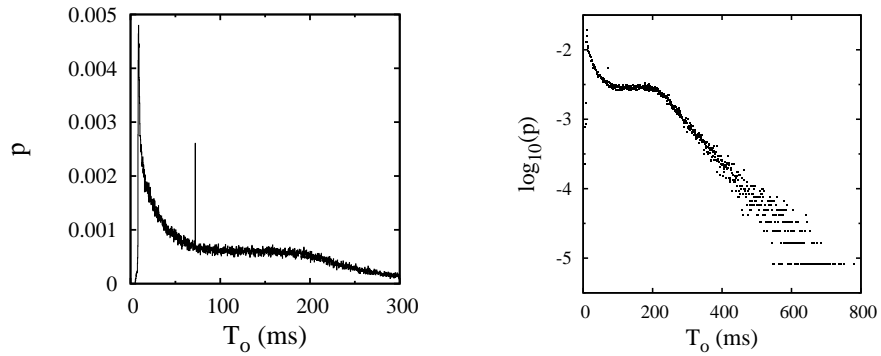


Figure 7.13: Left: The output ISI histogram for a Poisson input with average input ISI equal to 80 ms; Right: The same histogram on a log scale showing exponential tail of the distribution. At intermediate frequencies the distribution is not Poissonian. The origin of the time axis is set at the arrival of the first spike of the stimulus. Here  $g_{syn} = 0.34\text{mS}/\text{cm}^2$ .

Fig. 7.14 shows the return map for the Poisson input with the mean ISI of 80ms. This type of map indicates a negative first-order serial interval coefficient which cannot be described by renewal processes [Koch, 1999] and is typical of neurons having some mechanism of spike frequency adaptation. The serial correlation coefficient of order  $j$  is  $\rho_j = C_j/\sigma^2$ , where  $C_j = E[(T_n - \bar{T}_o)(T_{n+j} - \bar{T}_o)]$

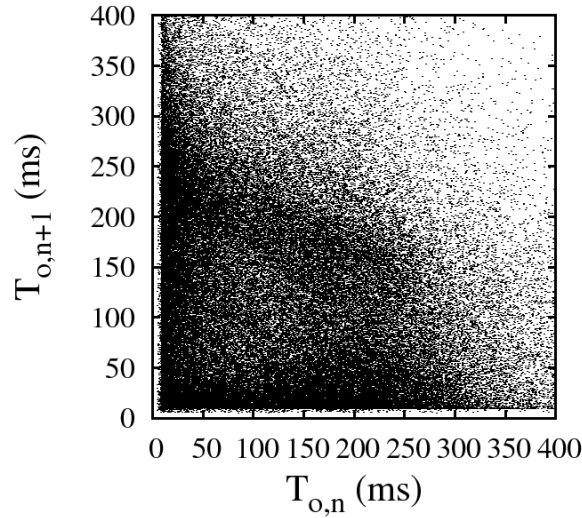


Figure 7.14: The return map of the output ISI for a Poisson input with the mean input ISI equal to 80ms.

is the covariance of intervals of lag  $j$ ,  $E$  denotes the expectation value, and  $\sigma$  is the standard deviation.  $\bar{T}_o$  is the average output ISI.

Our model differs from the procedure used by Harsch and Robinson [Harsch and Robinson, 2000] for cells from the rat visual cortex and cannot be compared directly. However we believe that the qualitative similarity of the return map, the CV, the firing variability and the precision indicate similar cell dynamics. We showed here that even a perfectly periodic input may lead to moderate variability with the CV up to 0.4 – 0.5. This is consistent with conclusions of the experimental work in Ref. [Harsch and Robinson, 2000].

The average oscillation frequency as a function of the signal amplitude is shown in Fig. 7.15 (left). The frequency calculated using the voltage peaks exceeding 0mV shows nearly periodic dependence on  $g_{syn}$  and the maximum  $f_o \approx 30\text{Hz}$ , a nearly 1.5 increase over the average input frequency  $f_i = 20\text{Hz}$ . The coefficient of variation has the same nonmonotonic dependence on  $g_{syn}$  (see Fig. 7.15 (right)).

The maxima of  $f_o$  are due to the presence of bursts. Two subsequent spikes are defined as being part of a burst if their separation is less than  $T_{i/2}$ . The maxima of  $f_o$  and  $T_b$  coincide. The peaks of  $f_o$  may be labeled by the average number of peaks in a burst. At the first maximum there are two peaks in a burst. Each of the consecutive maxima contains one more subleading peak per burst relative to the previous maximum. This type of resonant effect allows selective response only to those signals that have both the preferred frequency and strength.

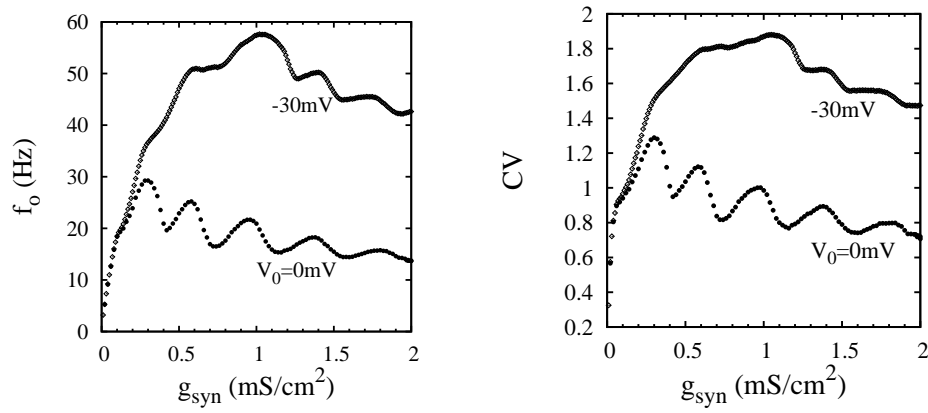


Figure 7.15: The average output frequency and the coefficient of variation as a function of  $g_{syn}$ , for average input frequency  $f_i = 20\text{Hz}$ , counting peaks with  $V_{max} > -30\text{mV}$  and  $0\text{mV}$ .

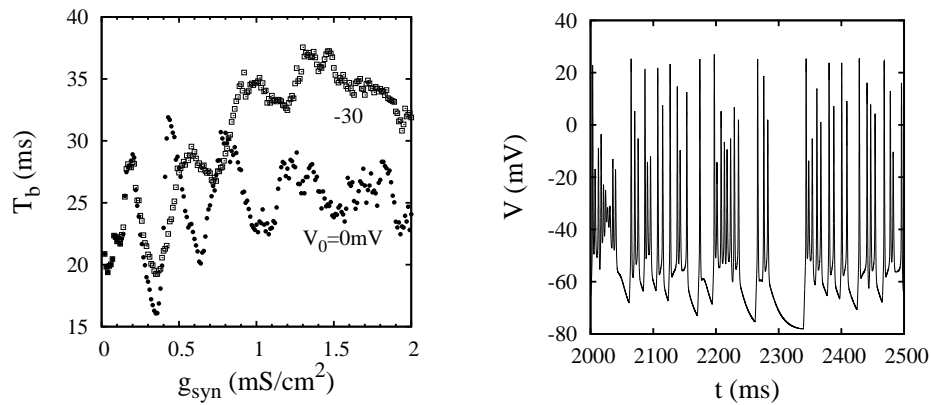


Figure 7.16: The average duration of bursts (left) as a function of  $g_{syn}$  for average  $T_i = 50\text{ms}$ , for two choices of the peak voltage,  $V_{max} > -30\text{mV}$  and  $0\text{mV}$ . Low amplitude components contribute more significantly for larger  $g_{syn}$ . A sample voltage trace at average  $T_i = 50\text{ms}$  and  $g_{syn} = 0.3\text{mS/cm}^2$  is shown on the right.

Fig. 7.16 presents average duration of bursts and a sample voltage trace, where it is clear that relatively long periods of quiescence alternate with bursts. Harsch and Robinson found in their experimental study [Harsch and Robinson, 2000] that an increased synchrony of unitary input events led to greater variability and reached levels typically recorded *in vivo*. The increase of CV was associated with the longer duration of bursts. Results in Figs. 7.15 (right) and 7.16 (left) agree with experiment. The highest variability is related to the presence of the longest bursts. While the stimulus in our calculation was different

from the one used in Ref. [Harsch and Robinson, 2000], the similarity of results is a consequence of the same neuronal dynamics.

The nonmonotonic dependence of  $f_o$  on  $g_{syn}$  may be used in the filtering of signals of a preferred amplitude. The highest output frequency is obtained at intermediate  $g_{syn}$ . This preferential response to stimuli of intermediate strength may be part of the homeostatic mechanism in cortical networks. In a network this effect may give preference to correlated inputs from certain groups of neurons. Also it would prevent the network from overload, filtering out excessively large stimuli by slowing oscillations of synchronizing neurons. The regular spiking inhibitory neuron studied here is most likely to stabilize oscillations in the gamma band.

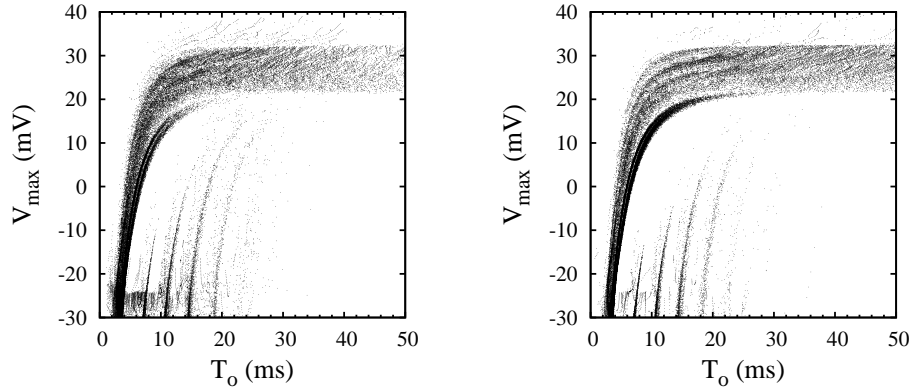


Figure 7.17: The output peak voltage vs. ISI for average input  $T_i = 20\text{ms}$  (left) and  $T_i = 50\text{ms}$  (right), when  $g_{syn}$  is varied between 0 and  $2\text{mS}/\text{cm}^2$ . There is a high-frequency bursting subresonance with  $f \sim 250\text{Hz}$ .

Fig. 7.17 shows voltage peak maxima vs. length of the preceding ISI. The resonances separated by approximately 4ms come from bursts of less-pronounced peaks which follow the leading voltage peak. The existence of such high-frequency ISIs is necessary in neurons performing the synchronization between groups of neurons [Whittington et al., 2000]. More precisely, the intrinsic dynamics of a synchronizing neuron should contain frequencies larger than the neuron population frequency. If this condition is satisfied delays associated with the finite length of neurons are insignificant and do not prevent synchronization.

## 8. Summary

We considered the dynamics of the Hodgkin-Huxley neuron and related models of regular spiking cells in the mammalian cortex subject to periodic and stochastic stimuli. We found the multimodal behavior in the high-frequency regime of the HH model. The source of the multimodality is the intrinsic non-linearity of the system, resulting in a highly irregular, probably chaotic, response to a perfectly periodic train of stimuli. The competition between the odd and the even ISI modes leads to a multimodal transition between two regimes of different parity. This radical change of the parity of available modes has dramatic observable consequences. The mean firing rate has a minimum slightly above the transition and the coefficient of variation (CV) has a cusp singularity at the transition. The cusp is most pronounced near the excitation threshold, where CV may exceed 1.

The multimodal transition is a consequence of the main resonance. Reacting to a high-frequency input the neuron tries to respond with a resonant frequency. Often one low-order fundamental mode dominates the response. However, when two such modes compete, e.g. modes 3:1 and 2:1, and the signal is relatively weak, there may be no preferred response frequency.

The competition of modes of different parity is also reflected in the structure of the main resonance, where states with the dominant even or odd ratios of the output ISI to the input ISI alternate. They are separated by irregular response, which may be chaotic, as indicated e.g. by bifurcations. The even-odd crossover involves participation of higher-order modes. The irregular response near threshold is characterized by an almost linear relation between the synaptic coupling and the mean output frequency. Also CV is a linear function of  $g_{syn}$  in that regime.

The excitation threshold is not a sharp boundary but rather a complicated set of points. The same is true for boundaries of mode-locked states in various parts of the resonant regime. They often have fractal character. The most pronounced irregularities of these edges occur in the regions where the dominant modes  $k = 2$  and  $k = 3$  compete.

We also clarified the topology of the response diagram for short-pulse stimuli. The resonances at the excitation edge alternate with bistable regions. Each of the three resonance regimes identified in Chapter 3 consists of three major components: a dominant mode-locked plateau, a pocket of chaotic-like response, a sequence of mode-locked areas with frequencies of the locked states decreasing towards the edge. The dependence of frequency vs. stimulus am-

plitude is continuous or nearly continuous at the resonance and at chaotic-like states. In the conventional picture of a type 2 neuron it responds with a finite frequency when the stimulus exceeds certain minimum value. In view of our results this description should be revised. The frequency-amplitude relation is clearly discontinuous only at some intervals along the excitation boundary. The topology of this set may be quite complicated. It was recognized earlier that noise smoothes the  $f-I$  relationship. We showed that the intrinsic nonlinearities of the neuron have similar effect and the functional form of the time dependence of the signal strongly influence this property.

The presence of noise lowers the excitation threshold. In many areas of the response diagram the output frequency has a minimum as a function of noise intensity. This effect is due to participation of higher ISI modes as a result of trajectory switching influenced by noise. We found a stochastic coherence anti-resonance near the deterministic multimodal transition where strongly irregular, chaotic-like dynamics dominates the response. The average response frequency has a minimum at small noise and CV has a maximum. The anti-resonance may be viewed as a companion effect to the multimodal transition.

Small amount of noise regularizes the average deviation from the perfect mode-locking,  $k - k_n$ , near the right edge of mode-locked plateaus. It becomes linear as a function of  $g_{syn} - g_c^+$ , where  $g_c^+$  is the value of  $g_{syn}$  at the edge.

For inputs consisting of isolated spikes or clusters of spikes the neuron's response is very sensitive to the width of the stimulus. It is convenient to scale the signal by the charge transferred by one such cluster. For stimuli much shorter than the main resonance period the details of the time dependence do not matter. Scaled excitation threshold of short stimuli with different time dependence is almost a universal function of stimulus width. There is a well-pronounced minimum of the scaled threshold at cluster widths of order 5 or 6ms. The preferred stimulus width is given approximately by the difference of the main resonance period and the refractory time. The optimal time scale of signal processing by such neuron may be of the same order of magnitude. The initial few milliseconds of response contain information about the entire neuron's dynamics. This would help to explain the speed of decision making in living organisms, where often the reaction time from the onset of stimulus is of order 30 to 100 ms.

We also studied the HH neuron's dynamics in a network setting, assuming the neuron receives input from 100 up to 1200 other HH neurons. At low frequencies CV grows approximately linearly with decreasing  $f$ , reaching values of order 1 which is of the same order as observed *in vivo* in measurements of the cortical activity in mammals. Near the excitation threshold the multimodal ISI distribution evolves into a bimodal form, indicating proximity to a bistable solution. This phenomenon is associated also with a high CV obtained in the same calculations. The growth of CV is due to the switching between bursts and longer periods of silence. The high variability of output by a single neuron participating in such network comes from the cell's intrinsic nonlinearity, independently of the geometry of connections and details of the signal's time

dependence. The anti-resonance related to the multimodal odd-all transition of a single neuron is preserved in the network.

We characterized the response of two classes of regular spiking pyramidal neurons in the neocortex of mammalian brains. Both excitatory and inhibitory neurons have a resonance at high frequencies. The dynamics of the inhibitory neurons is much richer due to the presence of an inhibitory channel which introduces additional time scale. The short-term response for  $t < 200\text{ms}$  from the onset of stimulus is typically regular and different from the long-term behavior. The average frequency, the bursting period and CV are oscillatory functions of the stimulus amplitude which is related to the appearance of additional spikes following the main one. These subleading spikes have smaller amplitude and are associated with a high-frequency subresonance at  $f_{res} \simeq 250\text{Hz}$ . The high- $f$  component is useful in overcoming transmission delays during synchronization of populations of neurons. The bursting frequency sets also the upper limit for the incoming signal oscillations. The neuron is not likely to respond to input frequencies exceeding  $f_{res}$ .

## Bibliography

- C. M. Armstrong and F. Bezanilla. *J. Gen. Physiol.*, 70:567–590, 1977.
- W. Bair and C. Koch. *Neural Comput.*, 8:1185–1202, 1996.
- A. L. Benabid, P. Pollak, C. Gervason, D. Hoffmann, D. M. Gao, M. Hommel, J. E. Perret, and J. de Rougemont. *Lancet*, 337:403, 1991.
- F. Bezanilla and C. M. Armstrong. *J. Gen. Physiol.*, 70:549–566, 1977.
- U. S. Bhalla and J. M. Bower. *J. Neurophysiol.*, 69:1948–1965, 1993.
- H. A. Blair. *J. Gen. Physiol.*, 15:709–729, 1932a.
- H. A. Blair. *J. Gen. Physiol.*, 15:731–755, 1932b.
- P. C. Bressloff and S. Coombes. *Phys. Rev. Lett.*, 81:2168, 1998.
- D. Brown, J. Feng, and S. Feerick. *Phys. Rev. Lett.*, 82:4731, 1999.
- G. T. Buracas, A. Zador, M. R. DeWeese, and T. D. Albright. *Neuron*, 20:959–969, 1998.
- Y.-Q. Che, J. Wand, W.-J. Si, and X.-Y. Fei. *Chaos, Solitons Fractals*, 39:454, 2009.
- D. T. W. Chik, Y. Wang, and Z. D. Wang. *Phys. Rev. E*, 64:021913, 2001.
- J. R. Clay. *J. Neurophysiol.*, 80:903–913, 1998.
- J. R. Clay. *J. Comput. Neurosci.*, 15:43, 2003.
- J. R. Clay. *Prog. Biophys. Mol. Biol.*, 88:59, 2005.
- J. A. Connor and C. F. Stevens. *J. Physiol. (London)*, 213:21, 1971.
- J. K. Douglass, L. Wilkens, E. Pantazelou, and F. Moss. *Nature (London)*, 365:337–340, 1993.
- D. A. Doyle, J. M. Cabral, R. A. Pfuetzner, A. Kuo, J. M. Gulbis, S. L. Cohen, B. T. Chait, and R. MacKinnon. *Science*, 280:69, 1998.
- S. Druckmann, Y. Banitt, A. Gidon, F. Schurmann, H. Markram, and I. Segev. *Front. Neurosci.*, 1:7–18, 2007.
- P. Duchamp-Viret, L. Kostal, M. Chaput, P. Lansky, and J.-P. Rospars. *J. Neurobiology*, 65:97, 2005.
- J. R. Engelbrecht and R. Mirollo. *Phys. Rev. E*, 79:021904, 2009.
- G. B. Ermentrout, R. F. Galan, and N. N. Urban. *Phys. Rev. Lett.*, 99:248103, 2007.
- A. A. Faisal, L. P. J. Selen, and D. M. Wolpert. *Nat. Rev. Neurosci.*, 9:292, 2008.
- D. Ferster and N. Spruston. *Science*, 270:756, 1995.

- L. Gammaitoni, P. Haenggi, P. Jung, and F. Marchesoni. *Rev. Mod. Phys.*, 70:254, 1998.
- W. Gerstner. *Phys. Rev. E*, 51:738, 1995.
- R. E. Gross and A. M. Lozano. *Neurol. Res.*, 22:247, 2000.
- J. Guckenheimer and R. O. Oliva. *SIAM J. Appl. Dyn. Syst.*, 1:105, 2002.
- B. S. Gutkin, J. Jost, and H. C. Tuckwell. *Europhys. Lett.*, 81:2005, 2008.
- B. S. Gutkin, J. Jost, and H. C. Tuckwell. *Naturwissenschaften*, 96:1091–1097, 2009.
- A. Harsch and H. P. C. Robinson. *J. Neurosci.*, 20:6181–6192, 2000.
- H. Hasegawa. *Phys. Rev. E*, 61:718, 2000.
- N. Ho and A. Destexhe. *J. Neurophysiol.*, 84:1488, 2000.
- A. L. Hodgkin. *J. Physiol.*, 107:165, 1948.
- A. L. Hodgkin and A. F. Huxley. *J. Physiol. (London)*, 117:500, 1952.
- L. Hofmann, C. Hauptmann, and P. A. Tass. *BMC Neuroscience*, 10 (Suppl 1):P318, 2009.
- R. L. Honeycutt. *Phys. Rev. A*, 45:600–603, 1992.
- E. M. Izhikevich. *Int. J. Bifurcation Chaos*, 10:1171, 2000.
- D. T. Kaplan, J. R. Clay, T. Manning, L. Glass, M. R. Guevara, and A. Shrier. *Phys. Rev. Lett.*, 76:4074, 1996.
- W. M. Kirstler, W. Gerstner, and J. L. van Hemmen. *Neural Comput.*, 9:1015–1046, 2001.
- L. Kocarev and J. Szczepanski. *Phys. Rev. Lett.*, 93:234101, 2004.
- L. Kocarev, J. Szczepanski, J. M. Amigo, and I. Tomovski. *IEEE Trans. Circuits Syst. I, Reg. Papers*, 53:1300–1309, 2006.
- C. Koch. *Biophysics of computation*. Oxford University Press, New York, 1999.
- N. Kopell, G. B. Ermentrout, M. A. Whittington, and R. D. Traub. *Proc. Natl. Acad. Sci. U.S.A.*, 97:1867, 2000.
- H. Lecar and R. Nossal. *Biophys. J.*, 11:1048–1067, 1971a.
- H. Lecar and R. Nossal. *Biophys. J.*, 11:1068–1084, 1971b.
- S. G. Lee and S. Kim. *Phys. Rev. E*, 60:826, 1999.
- S. G. Lee and S. Kim. *Phys. Rev. E*, 73:041924, 2006.
- J. E. Levin and J. P. Miller. *Nature (London)*, 380:165, 1996.
- A. Longtin. *J. Stat. Phys.*, 70:309, 1993.
- A. Longtin, A. Bulsara, and F. Moss. *Phys. Rev. Lett.*, 67:656, 1991.
- S. Luccioli, T. Kreuz, and A. Torcini. *Phys. Rev. E*, 73:041902, 2006.
- Z. F. Mainen and T. J. Sejnowski. *Science*, 268:1503–1506, 1995.
- A. Manwani and C. Koch. *Neural Comput.*, 11:1797–1829, 1999a.

- A. Manwani and C. Koch. *Neural Comput.*, 11:1831–1873, 1999b.
- A. Manwani and C. Koch. *Neural Comput.*, 13:1–33, 2001.
- E. Marder, A. E. Tobin, and R. Grashow. *Prog. Brain Res.*, 165:193–200, 2007.
- C. C. McIntyre, M. Savasta, B. L. Walter, and J. L. Vitek. *J. Clin. Neurophysiol.*, 21:1, 2004.
- B. K. McNamara and K. Wiesenfeld. *Phys. Rev. A*, 39:4854, 1989.
- R. C. Muresan and C. Savin. *J. Neurophysiol.*, 97:1911, 2007.
- H. Nakahama, H. Suzuki, M. Yamamoto, and S. Aikawa. *Physiology and Behavior*, 3:745–752, 1968.
- L. G. Nowak, M. V. Sanchez-Vives, and D. A. McCormick. *Cereb. Cortex*, 7:487, 1997.
- E. V. Pankratova, A. V. Polovinkin, and E. Mosekilde. *Eur. Phys. J. B*, 45:391, 2005.
- D. Paydarfar, D. B. Forger, and J. R. Clay. *J. Neurophysiol.*, 96:3338–3348, 2006.
- A. Pikovsky and J. Kurths. *Phys. Rev. Lett.*, 78:775, 1997.
- M. Pospischil, M. Toledo-Gonzalez, C. Monier, Z. Piwkowska, T. Bal, Y. Fregnac, H. Markram, and A. Destexhe. *Biol. Cyber.*, 99:427, 2008.
- S. A. Prescott, S. Ratté, Y. D. Koninck, and T. J. Sejnowski. *J. Neurophysiol.*, 100:3030, 2008.
- J. Rinzel and R. Miller. *Math. Biosci.*, 49:27, 1980.
- J. E. Rose, J. F. Brugge, D. J. Anderson, and J. E. Hind. *J. Neurophysiol.*, 30:769, 1967.
- P. Rowat. *Neural Comput.*, 19:1215, 2007.
- M. Sahin and Y. Tie. *J. Neural Eng.*, 4:227–233, 2007.
- G. Schmid, I. Goychuk, and P. Hänggi. *Europhys. Lett.*, 56:22–28, 2001.
- E. Schneidman, B. Freedman, and I. Segev. *Neural comput.*, 10:1679–1703, 1998.
- T. J. Sejnowski. *Nature (London)*, 376:21, 1995.
- M. N. Shadlen and W. T. Newsome. *J. Neurosci.*, 18:3870–3896, 1998.
- M. Siebler, H. Koller, C. C. Stichel, H. W. Muller, and H. J. Freund. *Synapse*, 14:206–213, 1993.
- R. M. Siegel. *Physica D*, 42:385, 1990.
- C. K. Sim and D. B. Forger. *J. Biol. Rhythms*, 22:445–453, 2007.
- W. Softky and C. Koch. *J. Neurosci.*, 13:334–350, 1993.
- C. F. Stevens and A. M. Zador. *Nature Neuroscience*, 1:210–217, 1998.
- D. Strassberg and L. J. DeFelice. *Neural Comput.*, 5:843–856, 1993.
- N. Takahashi, Y. Hanyu, T. Musha, R. Kubo, and G. Matsumoto. *Physica D*, 43:318, 1990.
- T. Tateno and H. P. C. Robinson. *J. Neurophysiol.*, 95:2650–2663, 2006.
- P. H. E. Tiesinga, J. V. José, and T. J. Sejnowski. *Phys. Rev. E*, 62:8413, 2000.

- R. D. Traub and R. Miles. *Neuronal networks of the Hippocampus*. Cambridge University Press, Cambridge, 1991.
- J. L. Wessale, L. A. Geddes, G. M. Ayers, and K. S. Foster. *Ann. Biomed. Eng.*, 20:237–244, 1992.
- J. A. White, R. Klink, A. Alonso, and A. R. Kay. *J. Neurophysiol.*, 80:262–269, 1998.
- J. A. White, J. T. Rubinstein, and A. R. Kay. *Trends in Neurosci.*, 23:131–137, 2000.
- M. A. Whittington, R. D. Traub, N. Kopell, B. Ermentrout, and E. H. Buhl. *Int. J. Psychophysiol.*, 38:315–336, 2000.
- K. Wiesenfeld and F. Moss. *Nature (London)*, 373:33–36, 1995.
- B. A. y Arcas, A. L. Fairhall, and W. Bialek. *Neural Comput.*, 15:1715–1749, 2003.
- W. M. Yamada, C. Koch, and P. R. Adams. Multiple channels and calcium dynamics. In C. Koch and I. Segev, editors, *Methods in neuronal modeling*. MIT Press, 1989.